

AD-A056 250

LOCKHEED MISSILES AND SPACE CO INC PALO ALTO CALIF PA--ETC F/6 4/1
ASSESSMENT OF PROCESSES RELATED TO PLASMA IRREGULARITIES. (U)
DEC 77 J B CLADIS, L L NEWKIRK, G T DAVIDSON DNA001-77-C-0207

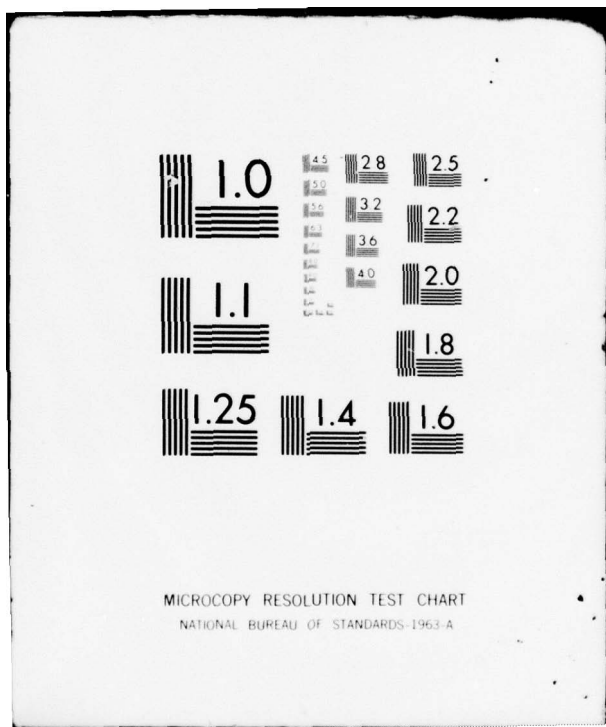
UNCLASSIFIED

DNA-4473F

NL

| OF |
AD
A056250

END
DATE
FILMED
8 -78
DDC



AD A 056250

(12)

LEVEL II

AD-E300 258

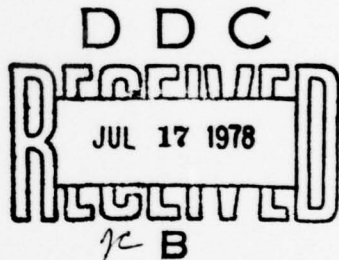
J

DNA 4473F

ASSESSMENT OF PROCESSES RELATED TO PLASMA IRREGULARITIES

Lockheed Palo Alto Research Laboratory
3251 Hanover Street
Palo Alto, California 94304

31 December 1977



Final Report for Period 15 May 1977–31 December 1977

DDC FILE COPY

CONTRACT No. DNA 001-77-C-0207

APPROVED FOR PUBLIC RELEASE;
DISTRIBUTION UNLIMITED.

THIS WORK SPONSORED BY THE DEFENSE NUCLEAR AGENCY
UNDER RDT&E RMSS CODE B322077462 T25AAXYX96004 H2590D.

Prepared for
Director
DEFENSE NUCLEAR AGENCY
Washington, D. C. 20305

78 06 07 021

Destroy this report when it is no longer
needed. Do not return to sender.



UNCLASSIFIED

SECURITY CLASSIFICATION OF THIS PAGE (When Data Entered)

REPORT DOCUMENTATION PAGE		READ INSTRUCTIONS BEFORE COMPLETING FORM
1. REPORT NUMBER DNA 4473F	2. GOVT ACCESSION NO.	3. RECIPIENT'S CATALOG NUMBER
4. TITLE (and Subtitle) ASSESSMENT OF PROCESSES RELATED TO PLASMA IRREGULARITIES		5. TYPE OF REPORT & PERIOD COVERED Final Report for Period 15 May 1977-31 December 1977
6. AUTHOR(s) J. B. Cladis W. E. Francis L. L. Newkirk M. Walt G. T. Davidson		7. CONTRACT OR GRANT NUMBER(s) DNA 001-77-C-0207 new
8. PERFORMING ORGANIZATION NAME AND ADDRESS Lockheed Palo Alto Research Laboratory 3251 Hanover Street Palo Alto, California 94304		9. PROGRAM ELEMENT, PROJECT, TASK AREA & WORK UNIT NUMBERS NWET Subtask T25AAXYX960-04
10. CONTROLLING OFFICE NAME AND ADDRESS Director Defense Nuclear Agency Washington, D.C. 20305		11. REPORT DATE 31 December 1977
12. MONITORING AGENCY NAME & ADDRESS (if different from Controlling Office) DNA, SBIE		13. NUMBER OF PAGES 74 (12) 68 p.
14. DISTRIBUTION STATEMENT (of this Report) 4473F AD-E 390 258		15. SECURITY CLASS (of this report) UNCLASSIFIED
16. DECLASSIFICATION/DOWNGRADING SCHEDULE		
17. DISTRIBUTION STATEMENT (of the abstract entered in Block 20, if different from Report)		
18. SUPPLEMENTARY NOTES This work sponsored by the Defense Nuclear Agency under RDT&E RMSS Code B322077462 T25AAXYX96004 H2590D.		
19. KEY WORDS (Continue on reverse side if necessary and identify by block number) Plasma Irregularities Electrostatic Potentials in Magnetosphere Trapped Radiation High Altitude Nuclear Effects Scintillations Plasma Instability Electric Fields Anomalous Resistivity		
20. ABSTRACT (Continue on reverse side if necessary and identify by block number) The occurrence of plasma irregularities that affect radio-wave propagation is assessed both for naturally-occurring disturbances and for disturbances resulting from a high-altitude nuclear explosion. Data obtained with the S3-3 satellite reveal that high electrostatic potential differences - to 8 kV - with associated plasma irregularities, often occur along the magnetic field at high latitudes. In a detailed analysis of electron and ion pitch-angle and energy distributions measured on the satellite, the potential differences		

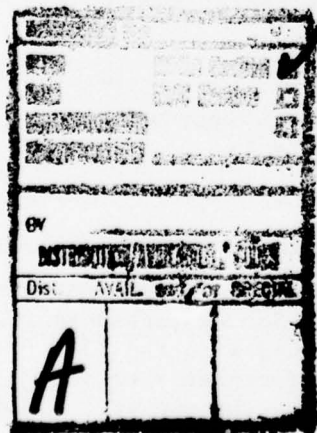
UNCLASSIFIED

SECURITY CLASSIFICATION OF THIS PAGE(When Data Entered)

20. ABSTRACT (Continued)

below and above the satellite, and the potential distribution above the satellite, were determined. The properties of the potential structure, together with concurrent observations of electrostatic waves, indicate that the potential is supported by anomalous resistivity. Analysis of the wideband data reveals that the scintillation activity has a spatial structure and occurrence similar to those of discrete auroral arcs and electric fields. The general morphology of the scintillations at high latitudes is described, and some interpretations of the data are suggested. The electric fields and currents induced by the debris plasma and fission beta-decay electrons in the magnetosphere due to a high-altitude nuclear explosion are estimated. For large bursts, the currents, both along and across the magnetic field, exceed well-established plasma-instability criteria, resulting in the formation of plasma irregularities. The region over which they are expected to occur extends as much as 60° in longitude east of the burst and, north of the burst, to latitudes near the auroral zone.

deg



UNCLASSIFIED

SECURITY CLASSIFICATION OF THIS PAGE(When Data Entered)

SUMMARY

Various processes are discussed that affect the electrical coupling of the ionosphere and the magnetosphere and the formation and distribution of plasma irregularities. The properties of electrostatic potential differences along magnetic field lines are inferred from analyses of the pitch-angle and energy distributions of the electrons and ions measured with the S3-3 satellite. Such potential differences, as high as 8 kV, appear about 70% of the time along field lines at latitudes $\gtrsim 65^\circ$. In a detailed analysis of an event observed at an altitude of 7280 km, invariant latitude $\sim 70^\circ$, 1800 MLT, 1054 UT on 15 September 1976, the potential differences below and above the satellite were deduced from the electron-distribution measurements. The total potential difference along the magnetic field was found to have an inverted-V type structure, increasing along the satellite path from zero to a maximum of about 4.3 kV and back to zero. The spatial extent of the structure in the north-south direction is about 340 km if it is assumed that the structure is stationary. Furthermore, the potential distribution above the satellite was estimated by computing the number densities of the electrons and ions from the measured fluxes and using the quasi-neutrality condition. The corresponding electric field was found to increase from zero at a distance of about 1460 km above the satellite to about 0.82 mV/m at the satellite. These results together with observations in that region of electrostatic waves with AC electric fields of ~ 10 mV/m indicate that the potentials are supported along the magnetic field by anomalous resistivity.

Data from the WIDEBAND satellite program were investigated with the intent of correlating scintillation activity with electron precipitation events and large-scale electric fields. The data obtained at mid-latitudes and at high latitudes are discussed. Certain types of scintillations are identified, and the morphology of the scintillations in the auroral regions is described. In general, scintillation activity has a spatial structure and occurrence similar to discrete auroral arcs and electric fields. Tentative interpretations are given for some of the observations.

38 06 07 021

It was found that widespread plasma irregularities may result from a high-altitude nuclear explosion. The electric fields and currents in the ionosphere-magnetosphere system resulting from the injection of debris plasma and fission beta-decay electrons were computed using a previously-developed model for the debris motion. The currents flow along the magnetic field lines at high altitudes and across magnetic field lines in the ionosphere. For bursts in the megaton range, it was found that both the field-aligned and cross-field currents become unstable and produce plasma irregularities. The pertinent plasma-instability criteria indicate that for bursts in the northern hemisphere the irregularities may occur over a wide region north and east of the burst. To the east the region may extend over a longitudinal sector approaching 60° ; to the north the region may reach the auroral zone.

PREFACE

We wish to thank Drs. R. G. Johnson, R. D. Sharp, and E. G. Shelley of the Lockheed Palo Alto Research Laboratory and Dr. J. F. Fennell of the Aerospace Corporation for making available to us their charged-particle data obtained on the S3-3 satellite. We also thank them for helpful discussions regarding the understanding of the data. We wish also to thank members of the Stanford Research Institute, particularly Drs. C. L. Rino, R. Vondrak, and O. de la Beaujardiere for furnishing us with Wideband data and assisting in its interpretation. Furthermore, we are grateful to Dr. C. R. Blank of the Defense Nuclear Agency for his guidance and support.

TABLE OF CONTENTS

<u>Section</u>		<u>Page</u>
	SUMMARY-----	1
	PREFACE-----	3
1	INTRODUCTION-----	7
2	COUPLING OF IONOSPHERE AND MAGNETOSPHERE	9
	2.1 Introduction	9
	2.2 Electric Potentials Inferred from Electron Measurements	10
	2.3 Distribution of Electric Potential Along Magnetic Field	24
	2.3.1 Number Density of Magnetospheric Electrons	26
	2.3.2 Number Density of Observed Electrons Moving Upward	29
	2.3.3 Number Density of Observed Protons Moving Upward	32
	2.3.4 Resultant Potential Distribution and Electric Field	33
	Appendix 2A Condition for Reflection of Electrons in Electric and Magnetic Fields	37
3	RELATIONS BETWEEN GEOPHYSICAL PHENOMENA AND IONOSPHERIC SCINTILLATIONS	39
	3.1 Introduction	39
	3.2 Mid-Latitude Observations	39
	3.3 High-Latitude Observations	41
	3.4 Morphology of Scintillations	54
	3.5 Discussion of Results	57
4	PLASMA IRREGULARITIES RESULTING FROM A H.A.N.E.	59
	4.1 Introduction	59
	4.2 Currents Due to Injected Debris	60
	4.3 Currents Due to Injected Electrons	61
5	REFERENCES	63

LIST OF ILLUSTRATIONS

<u>Figure</u>		<u>Page</u>
1	Schematic diagram of motion of satellite through region containing electrostatic potential	12
2	Counting Rate of CME A Detector	14
3	Counting Rate of CME B Detector	15
4	Counting Rate of CME C Detector	16
5	Pitch-Angle Data obtained on spins 1 and 3 by the CME D Detector	17
6	Electrostatic Potentials Along Magnetic Field inferred from pitch-angle and energy distributions of electrons measured on spins 1 through 4	21
7	Directional Flux of Protons	23
8	Electrostatic Potential and Electric Field	35
9	Number Densities of Electrons and Ions	36
10	Scintillation records for WIDEBAND pass 7-2	42
11	Scintillation records for WIDEBAND pass 5-37	43
12	Scintillation records for WIDEBAND pass 6-47	44
13	Scintillation records for WIDEBAND pass 5-36	45
14	Scintillation records for WIDEBAND pass 5-38	46
15	Scintillation records for WIDEBAND pass 6-8	47
16	Scintillation records for WIDEBAND pass 5-50	48
17	Scintillation records for WIDEBAND pass 5-51	49
18	Scintillation records for WIDEBAND pass 5-52	50
19	Scintillation records for WIDEBAND pass 7-42	51
20a	Morphology of high-latitude WIDEBAND scintillation	55
20b	Morphology of high-latitude WIDEBAND scintillation	56

TABLES

<u>Table</u>		<u>Page</u>
1	Energy Ranges of Electron Detectors	11
2	Parameters of Electron Flux Obtained by Fitting Spectral Form Given by Eq. (23) to Data	29

Section 1
INTRODUCTION

The degradation of radar and communications systems resulting from plasma irregularities in the ionosphere continues to pose a severe defense problem. Steady progress is being made on the understanding of the interference effects and on the prediction of the irregularity patterns due to naturally-occurring ionospheric disturbances. Several experimental programs, including the WIDEBAND experiment, are providing valuable information on the effects, and theoretical studies have identified several mechanisms that are responsible for some of the observed irregularities. The more perplexing problem, of course, is the prediction of the effects due to the irregularities resulting from a nuclear exchange. Some work has been done in that area. The known instability mechanisms have been applied to the problem. However, much more work is required. This report is on topics that are pertinent to the occurrence of irregularities in both the natural and nuclear-induced environments.

The electrical coupling of the ionosphere and the magnetosphere has an important influence on the formation and distribution of the irregularities. It affects the distribution of charged particles in the coupled regions, the energy deposition in the atmosphere, and the motions of the magnetic tubes that contain enhanced and striated plasma. The S3-3 satellite continues to provide the best available information on this problem. Our analysis of these data are described in Section 2. The data clearly indicate that for conditions above auroral arcs the electrical resistivity along the magnetic field is often many orders of magnitude (10^5) greater than the resistivity inferred from binary collisions. Hence, the usual assumption made in magnetospheric physics, that field lines are equipotentials, is not always valid. Potentials along the magnetic field as high as 8 kV are inferred from the measurements of the charged-particle fluxes obtained with S3-3 satellite. It appears that these potentials are due to plasma instabilities driven by field-aligned currents, but the data are not in agreement with the available theories. Much more information on this phenomenon is required in order to predict the effects which would result from a high-altitude nuclear explosion.

The following section, 3, describes our efforts to correlate the regions of scintillation activity with precipitation regions and large-scale electric fields. A sufficient amount of data from the WIDEBAND program are available to enable us to construct a picture of the general scintillation morphology in the auroral regions. In particular, we believe we can identify certain distinct regions of scintillation activity with the regions of auroral precipitation. The spatial structure and occurrence of these regions is similar to the structure and occurrence of discrete auroral arcs and electric field regions. It was not possible within the scope of the present work to make any detailed correlations, but the evidence is sufficient to indicate that the scintillation regions identified here are promising objects for further study.

The hot plasma - the nuclear debris and relativistic electrons - injected in the magnetosphere by a high-altitude nuclear explosion (H.A.N.E.) produces widespread electric fields and currents, both along and across the magnetic field, in the ionosphere-magnetosphere system. In our previous report (Ref. 1), the electric field induced by the atmospheric heave and the resulting current in the E-region of the ionosphere were estimated. The current was found to be unstable to the production of electrostatic waves, according to the Farley-Buneman mechanism. This instability forms magnetic-field aligned plasma irregularities; but, for this case, the instability is limited to distances in the ionosphere comparable to the dimensions of "heave" region. In Section 4 the electric fields and currents due to charge-separation processes in the magnetosphere resulting from the hot plasma injection are estimated. It is found that these currents are unstable in the same way, but over a much wider region. For bursts in the megaton range, the field aligned irregularities may extend north of the burst point to latitudes approaching the auroral regions and east of the burst to a longitudinal extent of about 60 deg.

Section 2
COUPLING OF IONOSPHERE AND MAGNETOSPHERE

2.1 INTRODUCTION

Until recently it was generally thought that quasi-steady electric fields could not be supported along magnetic field lines at altitudes above a few hundred kilometers. At those altitudes the collision frequencies of the charged particles with the neutral constituents of the atmosphere are very small. The mobilities of the charged particles along the magnetic field were therefore thought to be so high that the particles could rapidly become redistributed along the field in such a way as to neutralize any electric field that would tend to develop. However, as discussed in Ref. 1, several measurements of charged-particle fluxes in the auroral zones and a few observations of shaped-charge barium releases indicated the presence of high electric potentials along the magnetic field. At the present time the S3-3 satellite is providing valuable information on the nature of these potentials. They are observed in about half of the satellite passes at high latitudes, generally above auroral arcs (Ref. 2). Quite often these potentials are accompanied by field-aligned currents greater than 10^{-6} amps/m², broadband AC electric fields of tens of mV/m associated with electrostatic ion cyclotron waves (Ref. 3), and ions of ionospheric origin with energies of several keV (Ref. 4). These conditions indicate an anomalous resistivity along the magnetic field of about 100 ohm-m (plasma density ~100/cm³) compared with the classical resistivity of about 1.5×10^{-3} ohm-m (Ref. 5).

Fälthammar has reviewed recently the theories that have been proposed to explain the field-aligned potentials (Ref. 6). Two of these theories predict conditions which are in agreement with the data. Kindel and Kennel (Ref. 7) have shown that a field-aligned current with an intensity greater than about 10^{-6} Amps/m² and with a drift velocity that exceeds a certain minimum value is unstable to the production of electrostatic waves. Moreover, they showed that the instability favors the production of electrostatic ion cyclotron waves rather than acoustic waves; and, indeed, the data reveal that the electrostatic waves consist principally of the ion-

cyclotron waves. The interaction of the electrons carrying the current with the AC electric fields of the waves retards the electrons in a manner similar to collisions in a resistor. Accordingly, a potential builds up across this instability, or "anomalous resistivity", region. The DC electric field along the magnetic field must be smaller than the turbulent AC wave field (Ref. 6). Hence, since the observed wave field is typically 1-10 mV/m (Ref. 8), the expected DC electric field is of the order of 1 mV/m. The electric field due to anomalous resistivity must therefore extend several thousand kilometers along the magnetic field in order to account for the inferred potentials.

The other theory which is sometimes supported by the data was proposed by Block and Fälthammar (Ref. 9). They suggested that an electric double layer would result from a field-aligned current instability. The spatial extent of a double layer is small, being scaled in Debye lengths, but the electric field in the double layer is high. The measurements of Mozer et al. (Ref. 3) indicate the presence of high DC electric field intensities (~ 5 V/m) both along and across magnetic field lines, but the distribution of the field resembles the field expected for the paired oblique electrostatic-shock structure that has been proposed by Swift (Ref. 10). This is a modification of the double layer. The paired shocks are oblique to the magnetic field, and the electric field in the shock is more extensive, being scaled in ion gyroradii rather than Debye lengths.

In Section 2.2 the electron and ion fluxes observed with the S3-3 satellite through one of the field-aligned potential regions are discussed, and the analysis of the data that yields the potential differences below and above the satellite is described. In Section 2.3 the particle distributions based on the observations are transformed to altitudes above the spacecraft, assuming the particle motions to be adiabatic in the electric and magnetic fields, and the number densities of the particles are computed for assumed electric potential distributions. The potential distribution given by the quasi-neutrality condition is then determined and compared with the distributions predicted by theory.

2.2 ELECTRIC POTENTIALS INFERRED FROM ELECTRON MEASUREMENTS

In Ref. 1 we described the electrostatic potential differences along magnetic field lines inferred from an analysis of the pitch-angle and energy distributions of the electrons observed with the S3-3 satellite. The analysis was for an event observed at 1054 UT on 15 September 1976 at 18 hr MLT, 70° invariant latitude, and at an altitude of 7280 km. In reference 1 the analysis was done with an incomplete set of the data on the event. The further data has since been obtained. The results described below are based on an improved analysis of all of the data available on this event. Moreover, the analysis yields the distance over which the electrostatic potential extends above the spacecraft.

The motion of the satellite through the region sustaining the electric field is depicted in Figure 1. The satellite moved through this region toward higher latitudes. On successive spin periods, the satellite was located at the positions indicated by the numbers 1-4 in the figure.

The energy ranges of the four detectors used to observe the electrons are listed in Table 1.

Table 1
Energy Ranges of Electron Detectors

<u>Detector</u>	<u>Energy Range (keV)</u>
CME A	0.075 - 0.238
CME B	0.352 - 1.13
CME C	1.58 - 5.04
CME D	7.30 - 23.5

The counting rates of the detectors, on the various spin periods, as functions of the pitch-angle of the electrons are shown in Figures 2-5. Note that in Figures 2-4, the ordinates have been displaced by a decade to separate the curves. The pitch-angle notation is chosen such that electrons

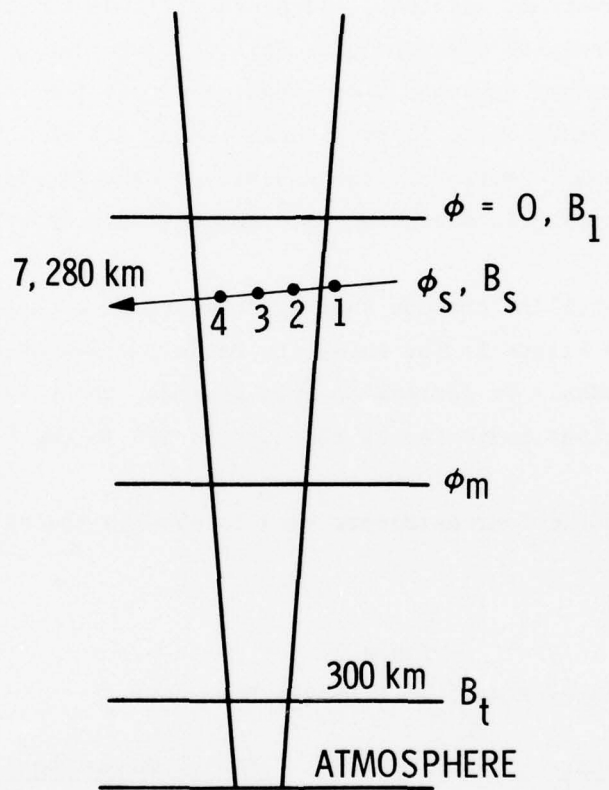


Figure 1 Schematic diagram of motion of satellite through region containing electrostatic potential (see text).

having pitch angles (α) of 0 and 180° move along the magnetic field toward and away from the near atmosphere, respectively. The numbers at the curves denote the spin number, and the superscripts - and + denote the 1st and 2nd pitch-angle scans that are made during each spin period. Since the counting rates of the highest-energy detector, CME D, were low, the counting rates shown in Figure 5 were averaged over the separate scans of the spin periods.

On spin 1 note that the counting rates of all of the detectors indicate that the electron flux was very nearly isotropic except for the loss cone due to the near atmosphere. The counting rates of the detectors had been the same for many spin periods preceding spin 1, and the electron flux was very closely represented by a Maxwellian distribution with a number density of 0.76 and a temperature of 0.8 keV.

On the succeeding spins the presence of the potential below and above the satellite is more clearly demonstrated by the CME B and CME C counting rates. In Figures 3 and 4 note that the loss cones become progressively wider and deeper as the satellite moves from its position on spin 1 to that on spin 3. The edge of the loss cone, α_c , is related to the potential beneath the satellite through the conservation of the magnetic moment of the electrons, i.e.,

$$\frac{w_s \sin^2 \alpha_c}{B_s} = \frac{[w_s + q(\phi_m - \phi_s)]}{B_t} \quad (1)$$

or

$$\alpha_c = \sin^{-1} \left[\frac{B}{B_t} \left(1 + q \frac{(\phi_m - \phi_s)}{w_s} \right) \right]^{1/2} \quad (2)$$

Here, w_s and B_s are the electron energy and the magnetic field intensity at the satellite, q is the absolute value of the electron charge, and $\phi_m - \phi_s$ is potential difference between the satellite and limiting point $B = B_t$ where the electron mirrors above the atmosphere before it suffers substantial collisions. Note in particular from Eq. (2) that for a fixed potential difference the loss-cone width, $\pi - \alpha_c$, increases as w_s becomes smaller. This effect is clearly demonstrated by the data in Figures 3 and 4.

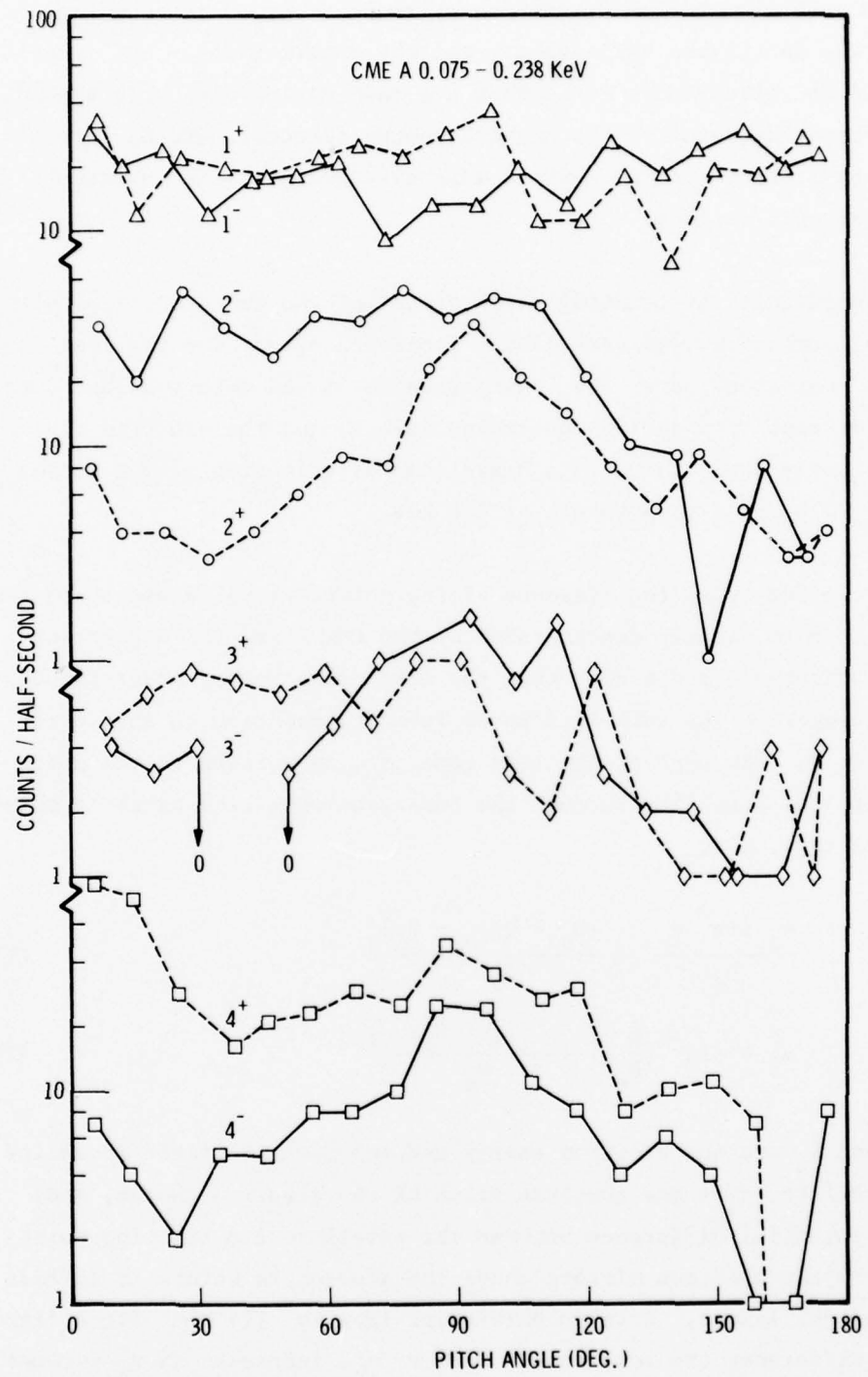


Figure 2 Counting rate of CME A detector as function of pitch angle. The numbers at the curves denote the satellite spin number, and the superscripts - and + denote the preceding and succeeding pitch-angle scans made during the satellite rotation.

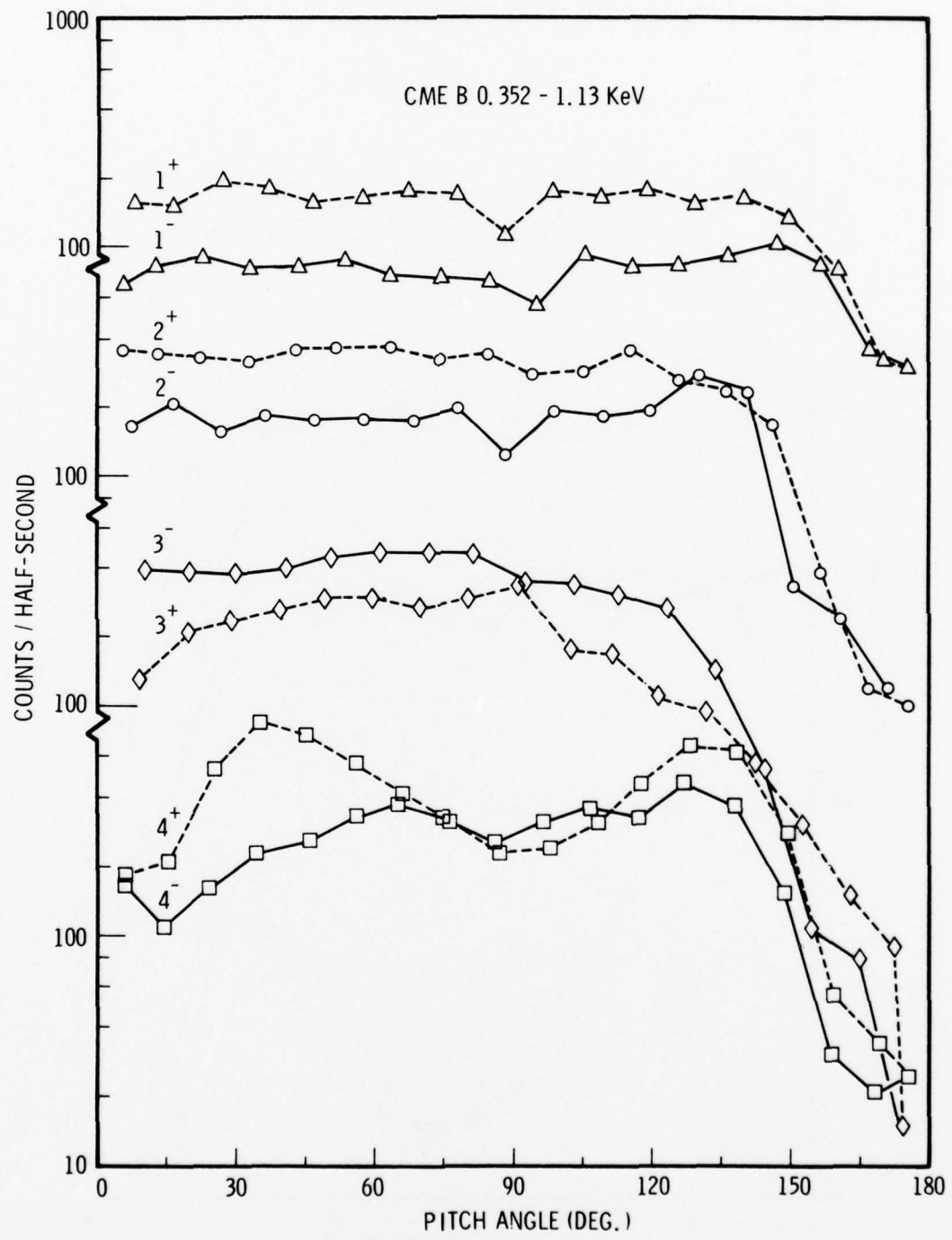


Figure 3 Counting rate of CME B detector as function of pitch angle. (See caption of Figure 1.)

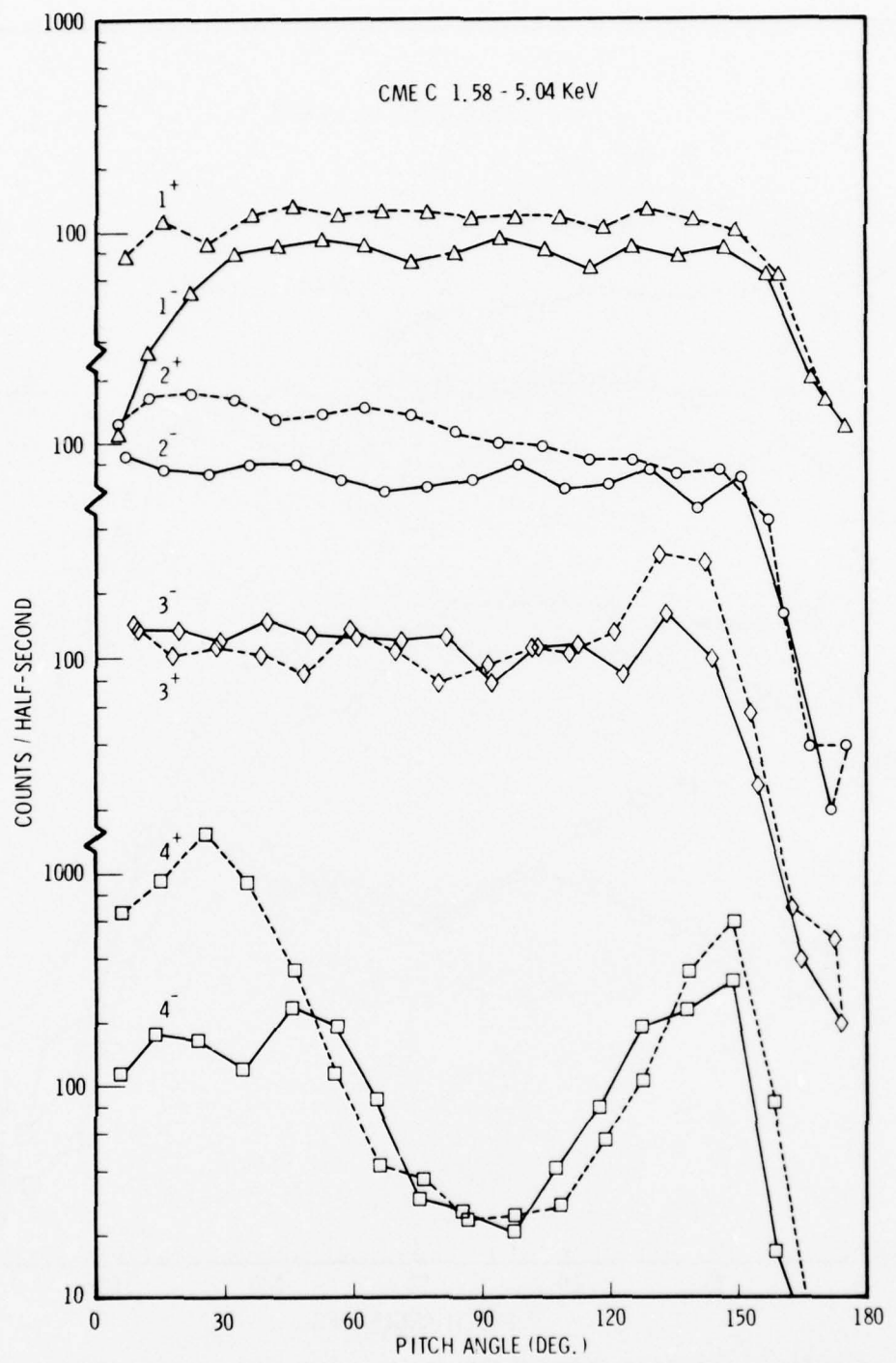


Figure 4 Counting rate of CME C detector as function of pitch angle. (See caption of Figure 1.)

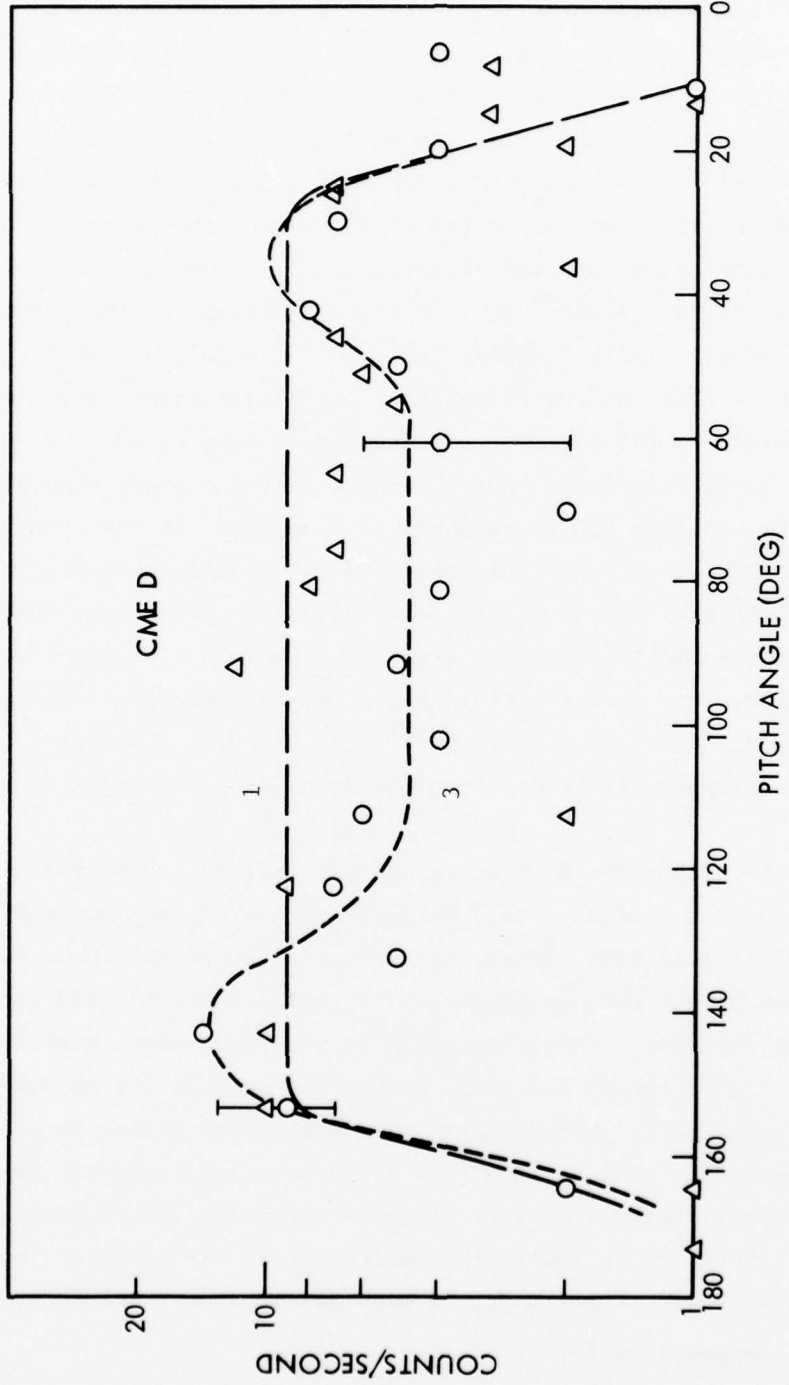


Figure 5 Pitch-angle data obtained on spins 1 and 3 by the CME D detector.

The loss cones become deeper as $\phi_m - \phi_s$ increases because the backscattered electrons have lower energies than the primaries, hence fewer of them can penetrate the retarding potential in order to reach the satellite.

The "butterfly" pitch-angle distributions on spin 4 indicate the presence of a potential difference above the satellite. The analysis described below indicates that as the spacecraft began its fourth spin (at the pitch angle $\alpha = 0^\circ$) the potential above the spacecraft, ϕ_s , had increased to about 0.8 kV and the field ratio B_1/B_s was about 0.77. This potential difference, by accelerating the electrons along the field, caused the pitch angles of the electrons to decrease, and the effect was more pronounced for the lower energy electrons. Accordingly, as shown in Figure 4, the counting rate of CME C was relatively constant from $\alpha = 0^\circ$ to 60° on scan 4⁻. All of the electrons within the energy range of the detector were detected at those pitch angles. As the detector continued to rotate toward $\alpha = 90^\circ$, it detected progressively lower fluxes because only the higher-energy electrons of the spectrum had the higher pitch angles. As the detector rotated from $\alpha = 90^\circ$ to $\alpha \approx 140^\circ$, it observed principally the electrons which were reflected by the magnetic field below the spacecraft; these electrons were primaries but with an augmented lower-energy component due to trapping between the electric field above the spacecraft and the magnetic field below. On the return scan (4⁺) the detector observed a higher fraction of the trapped electrons among the down-going electrons ($\alpha < 90^\circ$).

The counting rate of the CME B detector on spin 4 is due to different fractions of the electron sources. This detector responded to electrons in the range 0.352 to 1.13 keV. Hence, the potential above the spacecraft accelerated most of the primary electrons to energies which could not be observed by the detector. Here, the peaks in the pitch-angle distribution are due to the higher energy electrons within the sensitivity of the detector which are principally degraded primaries due to scattering in the atmosphere. Toward the minimum at $\alpha = 90^\circ$, the counting rates are due to progressively lower-energy electrons of the atmospheric backscatter. Again, the "symmetry" about 90° is due to the reflection of the electrons by the electric field above the spacecraft. A high fraction of these lower energy electrons are trapped locally.

The counting rate of detector CME A (See Fig. 2) beyond the second half of scan 2⁻ and just prior to the end of scan 4⁺ is principally due to locally-trapped and untrapped backscattered electrons. During that time the potential difference above the satellite exceeded the high-energy limit of the detector response (.238 keV). Hence, the primary electrons were accelerated to energies beyond the sensitivity region of the detector.

The detector CME D is not too useful in the analysis of this event because its response is to energies appreciably above the magnitudes of the potentials.

The energy ranges of the detectors (see Table 1) are too broad to resolve in sufficient detail the changes in the spectrum due to the potential and pitch-angle changes. Therefore, the following procedure was used to determine the potentials. The electron flux above the satellite, where the potential, ϕ , was zero and $B=B_1$ (see Fig. 1), was assumed to be the same as that measured on spin 1 at $B=B_s$. This assumption seems plausible because, as mentioned above, the electron flux measured on spin 1 was the same as it had been for many of the previous spin periods. A further assumption was that the electrostatic potential increased monotonically from $\phi = 0$ at B_1 to $\phi = \phi_m$ below the satellite, and remained constant, at ϕ_m , to the top of the atmosphere (300 km) where $B=B_t$ (see Fig. 1). The flux at $B=B_1$ was then transformed to the position of the satellite using Liouville's theorem for various values of B_1 , ϕ_s , and ϕ_m . This transformed flux included the downgoing electrons which arrived at the satellite directly from B_1 , the upgoing electrons which had mirrored below the satellite but above the "top" of the atmosphere, and the downgoing electrons which were reflected above the satellite by the repulsive potential - ϕ_s .

An iteration procedure was used to compute the equilibrium flux at the satellite due to the atmospheric backscatter for various values of B_1 , ϕ_s , and ϕ_m . First, the flux at B_1 was transformed to B_t where it was used as input to the AURORA code to compute the backscattered flux. Those electrons

which were reflected by the potential - ϕ_m were then added to the previously determined flux of electrons incident on the atmosphere, and the AURORA code was used again to compute the enhanced backscattered flux. The computations were continued in this manner until the backscattered flux converged to a constant value. Owing to the repulsive potential, - ϕ_s , above the satellite, the backscattered electrons contributed to the down-going fluxes at the satellite as well as to the upgoing fluxes.

The theoretical fluxes at the satellite were then integrated over the energy-response functions of the detectors, for various values of the electron pitch angles, and the resulting counting rates were compared with the experimental values. Those values of the electrostatic potentials below and above the spacecraft which brought the theoretical counting rates into agreement with the experimental values are shown in Figure 6. On spin 5 the electron and energetic-ion fluxes dropped off suddenly to the noise levels of the detectors indicating an absence of the potential. Hence, the analysis reveals an inverted-V type structure similar to the paired, oblique electrostatic shock structure proposed by Swift (Ref. 10) to explain various phenomena which have been observed in and above the auroral zones. However, important differences exist. The structure shown in Fig. 6, when transformed along field lines to an altitude of 100 km, has a north-south extent of about 70 km. This is much wider than structure proposed by Swift, which is comparable to the width of a discrete auroral arc. The observed width is closer to that inferred by Frank and Ackerson (Ref. 11) to explain the inverted-V shaped electron fluxes that they observed with the Injun 5 satellite at high latitudes. The energies of the electron fluxes observed by these experimenters at the apex of the structure are also consistent with the peak value of the potential shown in Fig. 6. Furthermore, the electric field along the magnetic field appears to be much smaller than that required by Swift's distribution: the mean value of the electric field can be estimated from the Spin 4 data which indicate a potential above the spacecraft of 0.8 kV over a magnetic-field ratio B_1/B_s of 0.77 (distance of 1460 km). These values imply a mean field of 0.8 kV/1460 km or ~0.5 mV/m. The analysis described in Section 2.3 provides further information about this electric field.

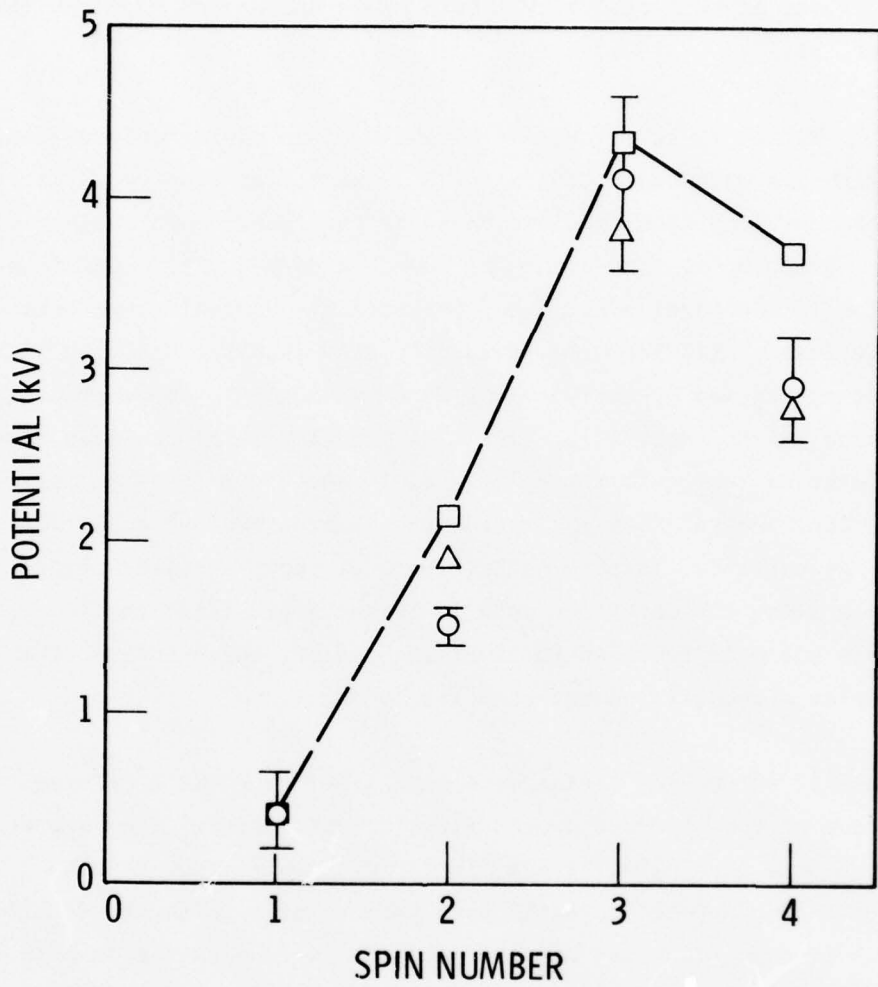


Figure 6 Electrostatic potentials along magnetic field inferred from pitch-angle and energy distributions of electrons measured on spins 1 through 4. The circles denote the best estimates of the potential difference below the satellite. The uncertainties of these values are indicated by the error bars. The triangles denote the potential difference below the satellite inferred from the depths of the loss cones alone. The squares denote the total potential difference, which includes the potential difference above the satellite.

As mentioned in the introduction, in some of these events the direct electric-field measurements indicate the presence of potential structures that are more nearly comparable to those described by Swift and with electric fields of hundreds of mV/m both along and across magnetic field lines (Ref. 3).

On spins 2, 3, and 4 high fluxes of H^+ and O^+ ions moving upward, closely aligned with the magnetic field ($\alpha > 170^\circ$), were also observed. The acceleration of ions from the ionosphere by the inferred potentials is expected. However, on this event the ion data do not yield additional information on the magnitudes of the potentials. Several complications can be mentioned. (i) The ions evidently also interact strongly with the electrostatic ion cyclotron waves which seem always to be present during these events (Ref. 13). (ii) The travel time of the ions along the acceleration region is appreciable (> 10 sec for a 1 keV proton), hence the ion spectrum does not reveal the "instantaneous" conditions below the spacecraft. (According to Figure 6, the potentials change appreciably along the satellite path in 10 sec.) And (iii) the ion spectra are not well resolved in time; each of the three ion spectrometers samples a specific energy step for 16 sec.

On this event, the O^+ ion fluxes were much lower than the H^+ fluxes. The spectrum of the observed proton flux, the directional flux averaged over the "source cone" ($170^\circ \leq \alpha \leq 180^\circ$) is shown in Fig. 7. The numbers at the data points are the spin periods over which the data were acquired. The open triangles are the data that were obtained on spin 4 by researchers of the Aerospace Corporation (Ref. 14) who had an ion detector on the same satellite. The curves drawn in the figure are the fluxes corresponding to Maxwellian distributions but only within the very restrictive pitch-angle range; the solid curve is for a "temperature" of 0.2 keV and the broken curves is for a "temperature" of 0.4 keV. The data seem to indicate that the protons are suffering anomalous collisions while being accelerated along the field, and perhaps also that "runaway" protons are being accelerated throughout the potential region.

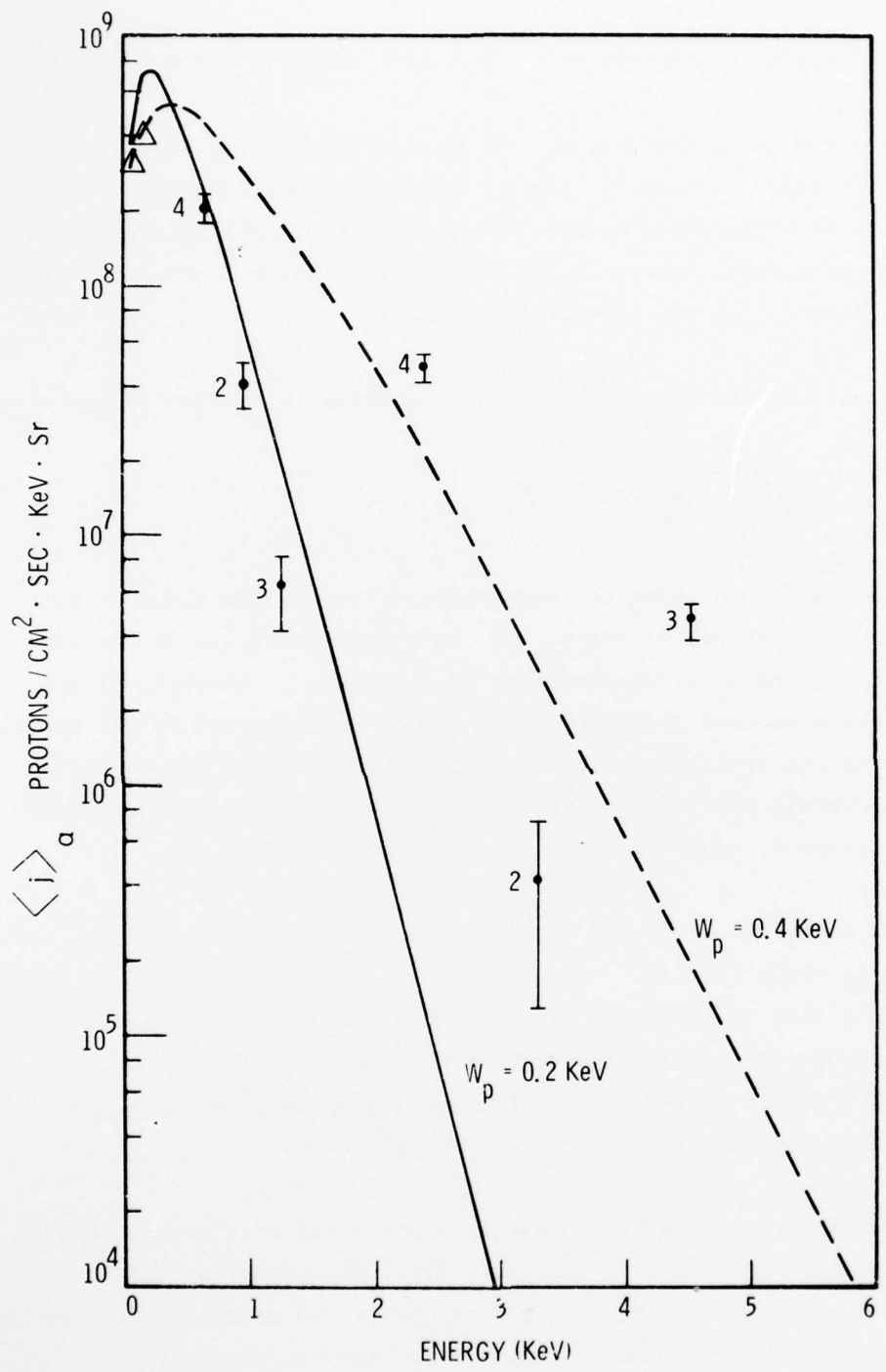


Figure 7 Directional flux of protons averaged over the 10-deg source cone as a function of the proton energy. The numbers at the points denote the satellite spin periods during the measurements. The triangles denote the data obtained by the Aerospace detector on the same satellite (Ref. 14).

2.3 DISTRIBUTION OF ELECTRIC POTENTIAL ALONG MAGNETIC FIELD

As discussed in the introduction, the distribution of the potential along the magnetic field provides a clue to the mechanism responsible for the potential. An attempt was made to estimate the potential distribution above the spacecraft, on spin 4, by computing the number densities of the ions and electrons in the potential region.

The potential distribution is given by a solution of Poisson's equation,

$$\frac{d^2\phi}{ds^2} = - \frac{q}{k_0} (n_i - n_e) \quad (3)$$

where s is a distance along the magnetic field, q is the absolute value of the electron charge, n_i and n_e are the number densities of the ions and electrons, and k_0 is permittivity of free space. However, if the scale of the potential distribution is large, as indicated by the analysis described in the previous section, the left-hand side of (3) is small, and the potential distribution can be estimated by finding that distribution that makes n_i equal to n_e (see, e.g., Persson, Ref. 15).

The number densities above the satellite ($B < B_s$) were computed for the following particle fluxes:

- (I) the flux of electrons moving downward from $B_1 < B$ which was assumed to be the same as that observed on spin 1,
- (II) the observed flux of electrons moving upward, and
- (III) the observed flux of protons moving upward.

The O^+ ion flux was neglected because, as mentioned previously, it was small in comparison to the proton flux. Also, the magnetospheric protons were not included in this analysis; essentially no magnetospheric protons were observed within the energy range of the ion spectrometers.

The general procedure was to transform the fluxes from B_s or B_1 to the region $B_s \geq B \geq B_1$ by using Liouville's equation,

$$\frac{j(w, \alpha, B)}{w} = \frac{j_b(w_b, \alpha_b, B_b)}{w_b} \quad (4)$$

where $w = w_b + \psi$ (5)

Here, j is the directional flux ($\text{number}/\text{cm}^2 \cdot \text{sec} \cdot \text{sr} \cdot \text{keV}$), the subscript $b=s$ or l refers to the quantities at the satellite ($B=B_s$) or at $B=B_1$ where $\phi=0$, and ψ is the energy gain or loss of the particles that move through the potential from B_b to B . The pitch angles are related through the conservation of the magnetic moment,

$$\frac{w \sin^2 \alpha}{B} = \frac{w_b \sin^2 \alpha_b}{B_b} \quad (6)$$

hence, $\alpha = \sin^{-1} \left[\frac{B}{B_b} \left(1 - \frac{\psi}{w} \right) \sin^2 \alpha_b \right]^{1/2}$ (7)

The number density was then computed by dividing j by the velocity v , which yields the number of particles/ $\text{cm}^3 \cdot \text{sr} \cdot \text{keV}$, and integrating over the appropriate ranges of α and w . Hence, by putting $v = (2w/m)^{1/2}$, the number density is given by the equation

$$n(B) = \left(\frac{m}{2} \right)^{1/2} \int dw \int \frac{j(\alpha, w, B)}{\sqrt{w}} 2\pi \sin \alpha d\alpha \quad (8)$$

The number densities were computed for a trial potential distribution $\phi(B)$, and the results for the ions and the electrons were compared over the full range $B_s \geq B \geq B_1$. The boundaries of $\phi(B)$ were maintained at the values given by the electron pitch-angle distributions, viz., $\phi(B_1) = 0$ and $\phi(B_s) = 0.8 \text{ kV}$. The computations were then repeated, using a different shape for $\phi(B)$, until the number densities of the ions and electrons were approximately equal. The computations were facilitated, as discussed below, by fitting the data with simple mathematical functions.

2.3.1 Number Density of Magnetospheric Electrons

The flux of electrons moving downward from B_1 is referred to here as the magnetospheric electrons (flux (I) listed above). As mentioned previously, this flux was assumed to be the same as that observed on spin 1. It was very closely represented by a Maxwellian velocity distribution with a number density n_o^e of $0.76/cm^3$ and a temperature w_e of 0.8 keV. The flux j at B_1 , corresponding to the Maxwellian distribution, may be written as

$$j_1(w_1, \alpha_1, B_1) = n_o^e k_e w_1 e^{-w_1/w_e}, \quad 0 \leq \alpha_1 \leq \frac{\pi}{2} \quad (9)$$

$$\text{where } k_e = (2\pi^3 m w_e^3)^{-1/2} \quad (10)$$

From Eqs. (4), (5), and (9), the flux at B transforms to

$$j(w, \alpha, B) = n_o^e k_e w e^{-(w-\psi)/w_e} \quad (11)$$

$$\text{where } w = w_1 + \psi(B)$$

$\psi(B) = q\phi(B)$ is the energy gained by the electrons. For electrons moving downward, $0 \leq \alpha \leq \pi/2$, the ranges of α and w for the integration (8) are obtained from Eq. (7). The are,

$$0 \leq \alpha \leq \alpha_H = \sin^{-1} \left[\frac{B}{B_1} \left(1 - \frac{\psi}{w} \right) \right]^{1/2}, \quad \psi \leq w \leq w_1 \quad (12)$$

$$0 \leq \alpha \leq \pi/2, \quad w > w_1$$

where

$$w_1 = \psi / (1 - B_1/B) \quad (13)$$

Hence, the number density of the downgoing electrons of the flux I is,

$$(n_e^e)^I_{\text{Downgoing}} = \frac{n_o^e \psi / w_e}{(\pi w_e^3)^{1/2}} \left\{ \int_{w_1}^{w_1} dw \left[\int_{\psi}^{\alpha_H(w)} e^{-w/w_e} \sqrt{w} \sin \alpha d\alpha \right] \right\}$$

$$+ \left\{ \int_{w_1}^{\infty} dw \left[\int_0^{\pi/2} e^{-w/w_e} \sqrt{w} \sin \alpha d\alpha \right] \right\} \quad (14)$$

$$(n_e^I)_{\text{Downgoing}} = \frac{n_0}{2} e \left\{ 1 - \text{Erf} \left[(\psi/w_e)^{1/2} \right] + \frac{2}{\sqrt{\pi}} (B/B_1 - 1)^{1/2} D \left[\left(\frac{\psi/w_e}{B/B_1 - 1} \right)^{1/2} \right] \right\} \quad (15)$$

Here, $D(x)$ is Dawson's integral:

$$D(x) = e^{x^2} \int_0^x e^{-t^2} dt \quad (16)$$

The number density n_e^I must include those electrons of flux I that are reflected at B' , where $B \leq B' \leq B_s$ and $\psi \leq \psi'(B') \leq \psi_s$. The electrons that are reflected at $B > B_s$ are included in the flux (II) listed above. The pitch angle at B of an electron that mirrors at B' is given by the equation,

$$\sin^2 \alpha_m = \frac{B}{B'} (1 + \frac{\psi'(B') - \psi(B)}{w}) \quad (17)$$

The upper limit of the pitch-angle integral in (8) for the reflected electrons is $\pi - \alpha_*(w)$ where $\alpha_*(w)$ is the minimum value of α_m for a given value of w . By differentiating (17) with respect to B' and setting the result equal to zero, the mirror point, B'_* , corresponding to α_* , is found to be at,

$$(\frac{d\psi'}{dB'})_{B'_*} = (w + \psi'(B'_*) - \psi(B))/B'_* \quad (18)$$

(In Appendix 2A at the end of this section, it is shown that the extreme value of (17) is a minimum only if $d^2\psi'/dB'^2 > 0$; but only such potential functions (positive curvature) have been found to give appropriate solutions.) Mathematical functions were used for $\psi(B)$, and a modification of Newton's method was used to solve (18) for B'_* . The value of α_* was

then computed by putting B'_* in Eq. (17). The minimum energy, w_* , given by Eq. (19) for electrons mirroring at B , is

$$w_* = B \frac{d\psi}{dB} \quad (19)$$

Hence, the number density of the upgoing electrons of flux I is,

$$(n_e^I)_{\text{upgoing}} = \frac{n_o e \psi / w_e}{(\pi w_e)^{3/2}} \int_{w_*}^{\infty} dw \int_{\pi/2}^{\pi - \alpha_*(w)} e^{-w/w_e} \sqrt{w} \sin \alpha d\alpha \quad (20)$$

This contribution to the number density was integrated numerically. Its magnitude given by the final iteration was also verified analytically by using a function $\phi(B)$ that closely approximated the final distribution in the range $0.8 \leq B/B_s \leq 1$ (see Section 2.3.4), but that also allowed (20) to be integrated in closed form. This function is given by the equation,

$$\phi = c (B/B_s - a) \quad (21)$$

Here $c = 3.72$ kV and $a = 0.785$. For this potential distribution, $B'_* = B_s$, $w_* = cB/B_s$, and the integration of (20) gives,

$$(n_e^I)_{\text{upgoing}} \approx \frac{n_o e}{2} \left(1 - \frac{B}{B_s}\right)^{1/2} \exp \left[- \frac{\psi_s B/B_s - \psi}{w_e (1 - B/B_s)} \right] \quad (22)$$

The final value of n_e^I is the sum of the components given in (15) and (20) or (22). Note that from (15) and (22), the value of n_e^I at B_1 ($\psi=0$) is,

$$n_e^I(B_1) \approx \frac{n_o e}{2} \left[1 + \left(1 - \frac{B_1}{B_s}\right)^{1/2} e^{-\frac{\psi_s / w_e}{B_s / B_1 - 1}} \right] \quad (23)$$

For $B_1/B_s = 0.77$ and $\psi_s = 0.8$ keV, the contribution to the number density by the reflected electrons from $(B_1 \leq B \leq B_s)$ is less than 2%. It is small because only the high-energy ($w > 3.72$ keV) electrons of the primary

distribution become reflected between B_1 and B_s . Note also that, as expected, if the potential ψ_s were zero and the magnetic mirror were very strong $B_1/B_s \rightarrow 0$, nearly all of the downgoing primaries would be reflected and n_e^I would approximately equal n_o^e .

Toward higher B values n_e^I decreases monotonically.

2.3.2 Number Density of Observed Electrons Moving Upward

The electron flux at the satellite with pitch angles in the range $90^\circ \leq \alpha \leq 180^\circ$ was estimated by fitting the functions,

$$j_{si}(w_s, \alpha_s, B_s) = n_i^e k_e w_s e^{-w_s/w_i}, \quad \alpha_{si}^L \leq \alpha_s \leq \alpha_{si}^H \quad (24)$$

to the data (Figures 2-5) in certain pitch-angle intervals. The "best fit" parameters n_i^e and w_i and the pitch-angle limits α_{si}^L and α_{si}^H are listed in Table 2.

Table 2
PARAMETERS OF ELECTRON FLUX OBTAINED BY
FITTING SPECTRAL FORM GIVEN BY EQ. (23) TO DATA

INDEX	n_i^e (cm^{-3})	w_i (keV)	α_{si}^L (Deg.)	α_{si}^H (Deg.)
1	1.55	0.35	90	110
2	1.85	0.45	110	120
3	2.10	0.59	120	138
4	1.43	0.61	138	148
5	0.50	0.70	148	158
6	0.20	0.50	158	180

Above the spacecraft the flux transforms to,

$$j_i(w, \alpha, B) = n_i^e k_e w e^{-(w + \chi)/w_i}, \quad \alpha_i^L \leq \alpha \leq \alpha_i^H \quad (25)$$

$$\text{where } w = w_s - \chi, \quad \chi = q(\phi_s - \phi) \quad (26)$$

For the upgoing electrons, the pitch-angle and energy limits given by the magnetic-moment conservation equation, are

$$\alpha_i^L = \sin^{-1} \left[\frac{B}{B_s} \left(1 + \frac{\chi}{w} \right) \sin^2 \alpha_{si}^L \right]^{1/2}, \quad w \geq w_1^i \quad (27)$$

and

$$\alpha_i^H = \sin^{-1} \left[\frac{B}{B_s} \left(1 + \frac{\chi}{w} \right) \sin^2 \alpha_{si}^H \right]^{1/2}, \quad w \geq w_2^i \quad (28)$$

where,

$$w_{1,2}^i = \frac{\chi g_i^{L,H}}{1 - g_i^{L,H}} \quad (29)$$

$$g_i^{L,H} = \frac{B}{B_s} \sin^2 \alpha_{si}^{L,H} \quad (30)$$

For $w_1^i \leq w \leq w_2^i$, the pitch-angle integration in (8) is from $\pi/2$ to α_i^L . For $w > w_2^i$ it is from α_i^L to α_i^H . By substituting (25) into (8) and performing the integration over the pitch angle, the number density may be written as,

$$n_e^{II} = \sum_{i=1}^6 \frac{n_i^e e^{-\chi/w_i}}{(\pi w_i^3)^{1/2}} \left\{ \begin{array}{l} \int_{w_1^i}^{w_1^i} [1 - (1 + \frac{\chi}{w}) g_i^L]^{1/2} e^{-w/w_i} \sqrt{w} dw \\ + \int_{w_1^i}^{\infty} \left([1 - (1 + \frac{\chi}{w}) g_i^L]^{1/2} - [1 - (1 + \frac{\chi}{w}) g_i^H]^{1/2} \right) e^{-w/w_i} \sqrt{w} dw + R_i \end{array} \right\} \quad (31)$$

where R_i represents the corresponding integrals for the electrons that are reflected by the electric field. For $w < \psi$, the electrons are reflected regardless of their pitch angle. Hence, for w_1^i and w_2^i less than ψ , R_i will include the integrals shown in (31) except that the upper limit of the second integral will be ψ . If only w_1^i is less than ψ , R_i will include only the first integral in (31) with the upper limit being ψ instead of w_2^i .

For $w > \psi$, the minimum pitch angle, α_* , of the reflected electrons will be determined as discussed in the previous section. If α_* is less than $\pi - \alpha_i^H$, the pitch-angle integration for R_i is from $\pi - \alpha_i^H$ to $\pi - \alpha_i^L$. If α_* is between $\pi - \alpha_i^H$ and $\pi - \alpha_i^L$, the integration is from α_* to $\pi - \alpha_i^L$.

The integrals appearing in (31) can be integrated as indicated in the previous section. Only the part of R_i for $w > \psi$ must be evaluated numerically. That part of R_i can also be integrated by using the approximate distribution given by Eq. (21). By using that function for ϕ , the integration of Eq. (31) yields,

$$\begin{aligned}
n_e^{II} = \sum_{i=1}^6 \frac{n_i^e}{2} & \left\{ (1-g_i^L)^{\frac{1}{2}} K\left(\frac{w_L^i - w_1^i}{w_i}\right) \exp\left(-\frac{x/w_i}{1-g_i^L}\right) \right. \\
& - (1-g_i^H)^{\frac{1}{2}} K\left(\frac{w_H^i - w_2^i}{w_i}\right) \exp\left(-\frac{x/w_i}{1-g_i^H}\right) \\
& + \frac{2}{\sqrt{\pi}} (B/B_1 - 1)^{\frac{1}{2}} \left[M\left(\frac{\psi_{si}^L}{w_i}\right) \exp\left(-\frac{\psi_s^L / w_i}{1-aS_L^i}\right) \right. \\
& \left. \left. - M\left(\frac{\psi_{si}^H}{w_i}\right) \exp\left(-\frac{\psi_s^H / w_i}{1-aS_H^i}\right) \right] \right\} \quad (32)
\end{aligned}$$

where

$$w_{L,H}^i = \psi + \frac{\psi_s a S_{L,H}}{1-S_{L,H}^i}; \quad S_{L,H}^i = \sin^2 \alpha_{si}^{L,H} \quad (33a)$$

$$K(x) = 1 + \text{Erf}(\sqrt{x}) - \frac{2}{\sqrt{\pi}} \sqrt{x} \exp(-x) \quad (33b)$$

$$M(x) = \sqrt{x} - D(\sqrt{x}) \quad (33c)$$

$$\psi_{si}^{L,H} = \psi_s \left(\frac{a}{1-a} - \frac{as_{L,H}^i}{1-a s_{L,H}^i} \right) \quad (33d)$$

and, again, $D(x)$ is Dawson's integral (Eq. 16). This equation was used to verify the numerical values in the region $0.8 \leq B/B_s \leq 1$.

2.3.3 Number Density of Observed Protons Moving Upward

The measurements of the proton flux were discussed in Section 2.2 and the data are shown in Figure 7. The curves in the figure are given by the function,

$$j_s(w_s, \alpha_s, B_s) = n_o^P k_p w_s e^{-w_s/w_p}, \quad 170^\circ \leq \alpha_s \leq 180^\circ \quad (34)$$

where

$$k_p = (2\pi^3 m_p w_p^3)^{-1/2} \quad (35)$$

The solid-line curve is for $w_p = 0.2$ keV and the broken-line curve is for $w_p = 0.4$ keV. Both of the curves have been normalized such that number density of the protons is equal to the sum of the number densities of the electrons ($n_e^I + n_e^{II}$) evaluated at $B=B_s$. The predominance of the data, especially when the Aerospace data on spin 4 are included, indicate that the solid-line curve is more representative of the average flux in the source cone.

Above the spacecraft this flux transforms to,

$$j(w, \alpha, B) = n_o^P k_p w e^{-(w-\chi)/w_p}, \quad \alpha_L \leq \alpha \leq \pi \quad (36)$$

$$\text{where } \chi = q(\phi_s - \phi) \quad (37)$$

is the energy gained by the protons, and

$$\alpha = \sin^{-1} \left[\frac{B}{B_s} \left(1 - \frac{\chi}{w} \right) \sin^2 \alpha_s \right]^{1/2}, \quad w \geq \chi \quad (38)$$

The limit α_L is given by (38) when $\alpha_s = \alpha_p = 170^\circ$.

In the case of the protons, there are no complications due to reflections because both the electric and the magnetic forces continually increase the proton velocities along the field.

After performing the pitch-angle integration in (8), the number density is given by the equation,

$$n_p^{III} = \frac{n_o^P e^{\chi/w_p}}{(\pi w_p^3)^{1/2}} \int_{\chi}^{\infty} \{1 - [1 - \frac{B}{B_s} (1 - \frac{\chi}{w}) \sin^2 \alpha_p]^{1/2}\} e^{-w/w_p} \sqrt{w} dw \quad (39)$$

$$= \frac{n_o^P}{2} e^{\chi/w_p} \left\{ 1 - \text{Erf} \left(\frac{\chi}{w_p} \right) - (1-g)^{1/2} e^{\frac{\chi}{w_p}} \frac{(g)}{1-g} [1 - \text{Erf} \left(\frac{\chi}{w_p(1-g)} \right)^{1/2}] \right\} \quad (40)$$

where $g = \frac{B}{B_s} \sin^2 \alpha_p$

Note that for $B=B_s$, $\chi = 0$,

$$n_p^{III}(B_s) = \frac{n_o^P}{2} (1 - \cos \alpha_p) \quad (41)$$

which is, as expected, equal to $n_o^P (\frac{\Delta\Omega}{4\pi})$, the number density due to a Maxwellian distribution times the fractional solid angle of the source cone. By equating $n_p^{III}(B_s)$ to $n_e^I + n_e^{II} = 1.711/\text{cm}^3$ at B_s , the value of n_o^P is found to be $225.2/\text{cm}^3$.

2.3.4 Resultant Potential Distribution and Electric Field

The number density of the protons was very nearly equal to the total number density of the electrons in the range $0.77 \leq B/B_s \leq 1$ for the potential distribution given by the equation,

$$\phi(B) = C_1 \left\{ \left[\frac{(B/B_s - 0.77)^2}{C_2^2} + 1 \right]^{1/2} - 1 \right\} \quad (42)$$

where $C_1 = 6.494 \times 10^{-2}$ kV and $C_2^2 = 2.999 \times 10^{-4}$. By differentiating (42) with respect to the distance along the magnetic field, assuming B to vary as the inverse-third-power of the geocentric distance, the electric field is found to be,

$$E = 3 \left(\frac{C_1}{C_2} \right)^2 \frac{B/B_s (B/B_s - 0.77)}{(R_s + S) (\phi(B) + C_1)} \quad (43)$$

Here, R_s is the geocentric distance to the satellite (13,660 km) and S is the distance above the satellite.

The potential distribution and the electric field are plotted in Figure 8 as a function of B/B_s . The number densities of the protons, n_p^{III} , and the electrons, $n_e^I + n_e^{II}$, resulting from this potential distribution are shown as a function B/B_s in Figure 9. Over the range of B/B_s from 1 to 0.83, the number densities were in agreement to within one part in 500. Toward lower magnetic field ratios, the number densities began to depart slowly with the number density of the electrons exceeding that of the protons.

As mentioned earlier, the end points of the potential distribution were fixed at those values given by the electron pitch-angle distributions (0.8 kV at B_s and 0 kV at $B_1/B_s = 0.77$). Only the shape of the distribution between those points was varied in this analysis. Nevertheless, since the number densities of the charges are quite sensitive to the distribution, it seems unlikely that appreciable departures from those end-point values would have given an equally good agreement of the number densities.

The measurements of Mozer et al. (Ref. 3) indicate that in the turbulent wave-field region, where such potentials appear, the number density of the thermal plasma may be as high as $50/\text{cm}^3$ with fluctuations of about 20%. Data on the plasma density for the event reported here were not obtained. However, even if the thermal plasma density was high, the preponderance of these particles as discussed in Section 2.1 are expected to be constrained from moving along the magnetic field by the local AC fields of the waves, which are tens of mV/m. The electric field shown in Figure 8 is less than about 1 mV/m. Of course, the runaway electrons and ions do move rapidly along the field, but the majority of these particles are probably included in the distributions used in this analysis.

The results shown in Figure 8 together with those in Figure 6 indicate that the potential distribution has a scale comparable to an earth's radius. Furthermore, the measurements of the Berkeley group (Ref. 16) on this event of the turbulent wave field and the field-aligned current indicate that the potential is supported by anomalous resistivity.

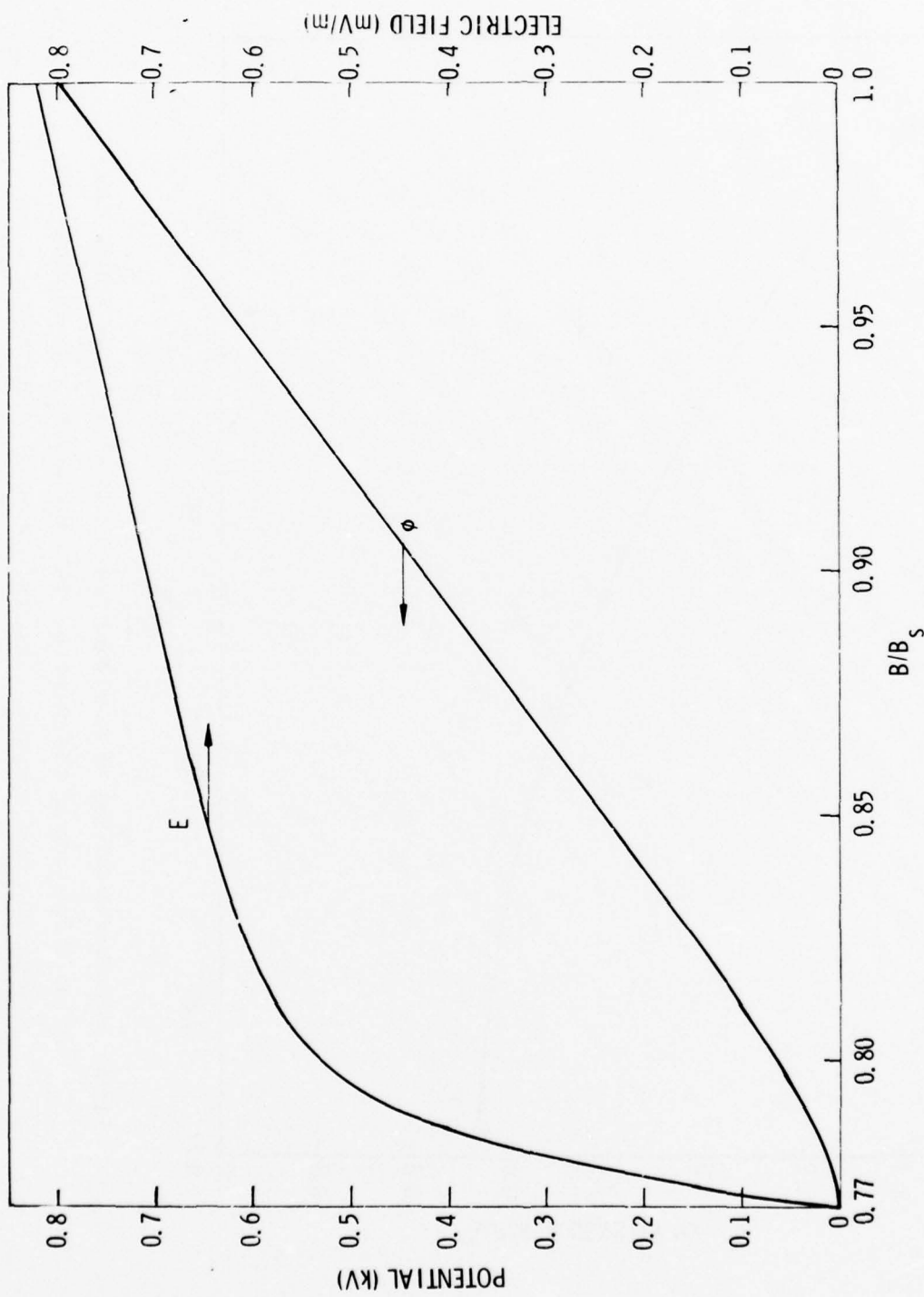


Figure 8 Electrostatic potential and electric field along the magnetic field as a function of the magnetic field ratio B/B_s .

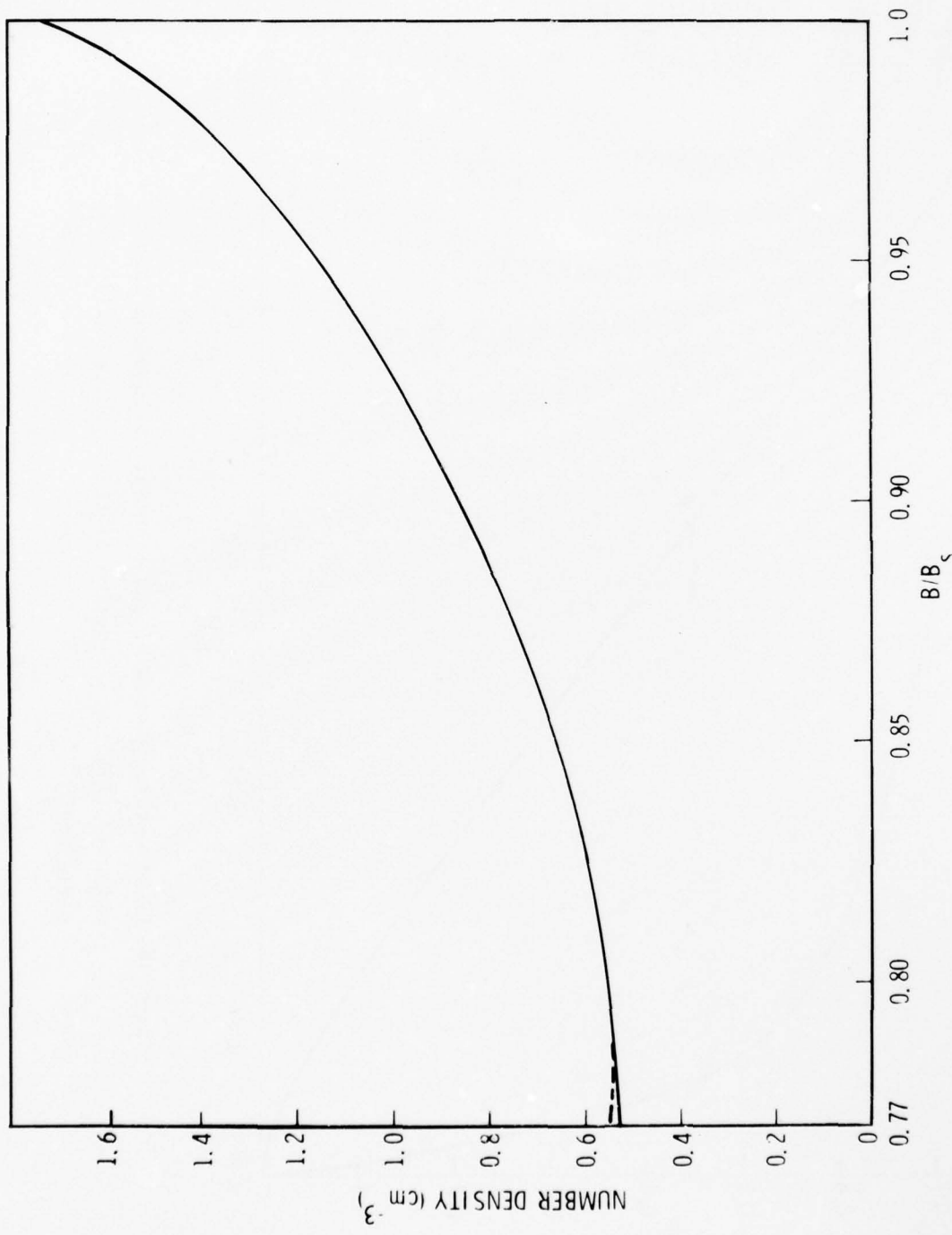


Figure 9 Number densities of electrons (dashed line) and ions (solid line) as a function of the magnetic field ratio B/B_s . These number densities were computed using the potential distribution shown in Figure 8.

APPENDIX 2A
CONDITION FOR REFLECTION OF ELECTRONS
IN ELECTRIC AND MAGNETIC FIELDS

If the energy, w , and magnetic moment, μ , of an electron are known at B where the potential is $q\phi=\psi$, the parallel component of the electron at B' where the potential is ψ'/q is given by the equation,

$$w'_{11} = w - \mu B + \mu(B-B') - (\psi-\psi') \quad (44)$$

Where, $w - \mu B$ equals w_{11} at B , $\mu(B-B')$ is the increase (or decrease) in w_{11} due to the change in B , and $\psi-\psi'$ is the decrease (or increase) in w_{11} due to the change in the potential.

The rate of change of w'_{11} with respect to B' , is, therefore,

$$\frac{dw'_{11}}{dB'} = -\mu + \frac{d\psi'}{dB'} \quad (45)$$

From this equation, it is clear that for upgoing electrons (B decreasing), the necessary condition for mirroring is $\frac{dw'_{11}}{dB'} > 0$, $B' > B'_m$, where B'_m is the mirror point. Thus, from (45)

$$\frac{d\psi'}{dB'} > \mu, B' > B'_m \quad (46)$$

Similarly, for downgoing electrons, the necessary condition for mirroring is,

$$\frac{d\psi'}{dB'} < \mu, B' < B'_m \quad (47)$$

Since $\mu = w \sin^2 \alpha / B$, the pitch angle at B for mirroring at B'_m , following from Eq. (44) for $w'_{11} = 0$, is given by the equation,

$$\sin^2 \alpha_c = \frac{B}{B'_m} \left(1 - \frac{\psi-\psi'}{w}\right) \quad (48)$$

The extreme value of α_c when plotted against B'_m occurs at the value of B' given by the equation,

$$\frac{d\psi'}{dB'_m} = \frac{w}{B'_m} \left(1 - \frac{\psi - \psi'}{w}\right) = \mu \quad (49)$$

A second differentiation of (46) reveals that at that point, α_c is a minimum or a maximum depending on whether the curvature of ψ' , $d^2\psi'/dB'_m^2$, is positive or negative, respectively.

As discussed in the text, potential functions with positive curvature were found to give appropriate results for the B range of interest. Hence, α_c was a minimum at the value of B'_m given by the solution of (49).

Section 3

RELATIONS BETWEEN GEOPHYSICAL PHENOMENA AND IONOSPHERIC SCINTILLATIONS

3.1 INTRODUCTION

The WIDEBAND satellite program, in operation now for over a year, has amassed a large body of data on the occurrence and morphology of ionospheric scintillations. The experiment consists mainly of a transmitter on a near-polar orbit, broadcasting on ten channels from VHF to S band [ref. 17]. The signals are received by stationary receivers in equatorial, mid-latitude, and auroral regions. The major shortcoming of the program is the absence of energetic particle detectors on the satellite. It has become clear from coordinated experiments with the Chatanika radar, rocket-borne instruments, and ground-based photometers [ref. 18], that there is a strong association between certain types of scintillation activity and particle precipitation. Efforts are underway, too, (by E. J. Fremouw and R. R. Vondrak of the Stanford Research Institute, and R. D. Sharp of Lockheed) to analyze the data from the occasional occurrences where the WIDEBAND data could be correlated with particle data from Lockheed instruments on the S3-3 satellite. In this report we will discuss some of the features of the scintillations and their apparent relationship to particle precipitation. A detailed analysis of selected individual cases is beyond the scope of the present work and will no doubt be treated by the above-cited workers.

3.2 MID-LATITUDE OBSERVATIONS

The first of many surprises in the WIDEBAND program was the high level of scintillation activity at mid-latitudes [ref. 17]. The receiver station at Stanford, California, was originally intended for checking out the operations; the location was selected solely because of its accessibility to the SRI laboratories. The period immediately after commencement of operations was very active (see Figure 20) so many good scintillation observations were observed at Stanford during the first two months [ref. 1]. However,

after four months of operation the Stanford receiving station was moved to an equatorial location. As explained in our last DNA report [ref 1], not enough data were accumulated at Stanford for statistical correlations with geophysical phenomena. We found no correlation with any of the important geomagnetic activity indices.

It is plausible that the mid-latitude scintillations are associated with precipitation from the trapped radiation belts, but, due to the lack of coordinated particle data, it has not been possible to test this supposition. The sporadic nature of the mid-latitude scintillations could be attributed to a number of possible causes. One factor that determines the spatial structure of the precipitation regions is the asymmetry of the geomagnetic field; drifting electrons tend to be precipitated in distinct longitude regions (e.g., the South Atlantic anomaly) [ref. 1]. The other important factor is the spatial distribution of the wave sources responsible for dumping electrons from the radiation belts. It has been suggested recently that man-made VLF emissions are very effective in causing energetic electron precipitation in mid-latitudes [ref 19]. Many of the naturally generated ELF/VLF emissions also show distinct preferences for certain local times. It may be concluded that more scintillation data are needed in mid-latitudes before meaningful statistical associations can be deduced.

It was our hope that high latitude wideband receiver stations (Poker Flat, Alaska) could be used to back up the mid-latitude observations by observing scintillations far to the south, in the mid-latitude regions. If the propagation path is assumed to intersect the scintillation region at 300 km altitude in the F-region ionosphere, the latitudinal coverage can readily be deduced. The limits of the coverage at Poker Flat were from about 50°N geomagnetic latitude to beyond 80° geomagnetic latitude. However, the scintillation indices increase directly with the total electron content along the propagation path. This, together with the difficulty of distinguishing spatial structures near the horizon, limited the southward coverage to about 58°N geomagnetic, which is near the northern limit of the plasmasphere.

It was therefore not practical to use the Poker Flat data for routine observations of mid-latitude regions. It does appear that the mid-latitude scintillations observed at Poker Flat were similar in character to those observed at Stanford. There was no readily discernible pattern that might be correlated with geomagnetic activity.

3.3 HIGH-LATITUDE OBSERVATIONS

The scintillation records show dramatic changes in character as they pass from mid-latitude through the plasma trough into the auroral zone. Figures 10 through 19 [courtesy C. L. Rino of Stanford Research Institute] show some sample scintillation records from the Poker Flat station; they are not necessarily typical, but were selected to illustrate certain features. Figure 10 shows a quiet pass. Starting at the right there is perhaps some activity at mid-latitudes in both phase (solid line) and amplitude scintillations (dashed line). There is only a weak correlation (if any) between the phase and amplitude scintillations on the right sides of these figures; that may be true of most of the mid-latitude observations. The second part of the figure shows the relative-phase scintillations in VHF, UHF, and L band; this record is of value mainly in indicating where the VHF records are suspect, as at the right side of Figure 10. The bottom part of the figure shows the total electron content integrated along the propagation path. The deep minimum shows clearly the location of the plasma trough which is expected at the southern edge of the auroral zone. The record in Figure 10 shows weak enhancement of the electron density on the poleward edge of the trough, and a slight amount of scintillation activity probably associated with aurorae beyond 63° geomagnetic latitude. One of the scintillation spikes here is probably spurious because the propagation path is nearly aligned with the field lines; this condition is usually noted by a tick mark on the plot of BP angle, here at 17.7° . At low and moderate levels of scintillation activity the activity is concentrated near the poleward edge of the plasma trough and is well correlated with local geomagnetic indices [communication from C. L. Rino]. There also seems to be some correlation between the phase and amplitude scintillation indices for this type of activity. Figure 11 shows an active pass and illustrates singular features: plasma trough with

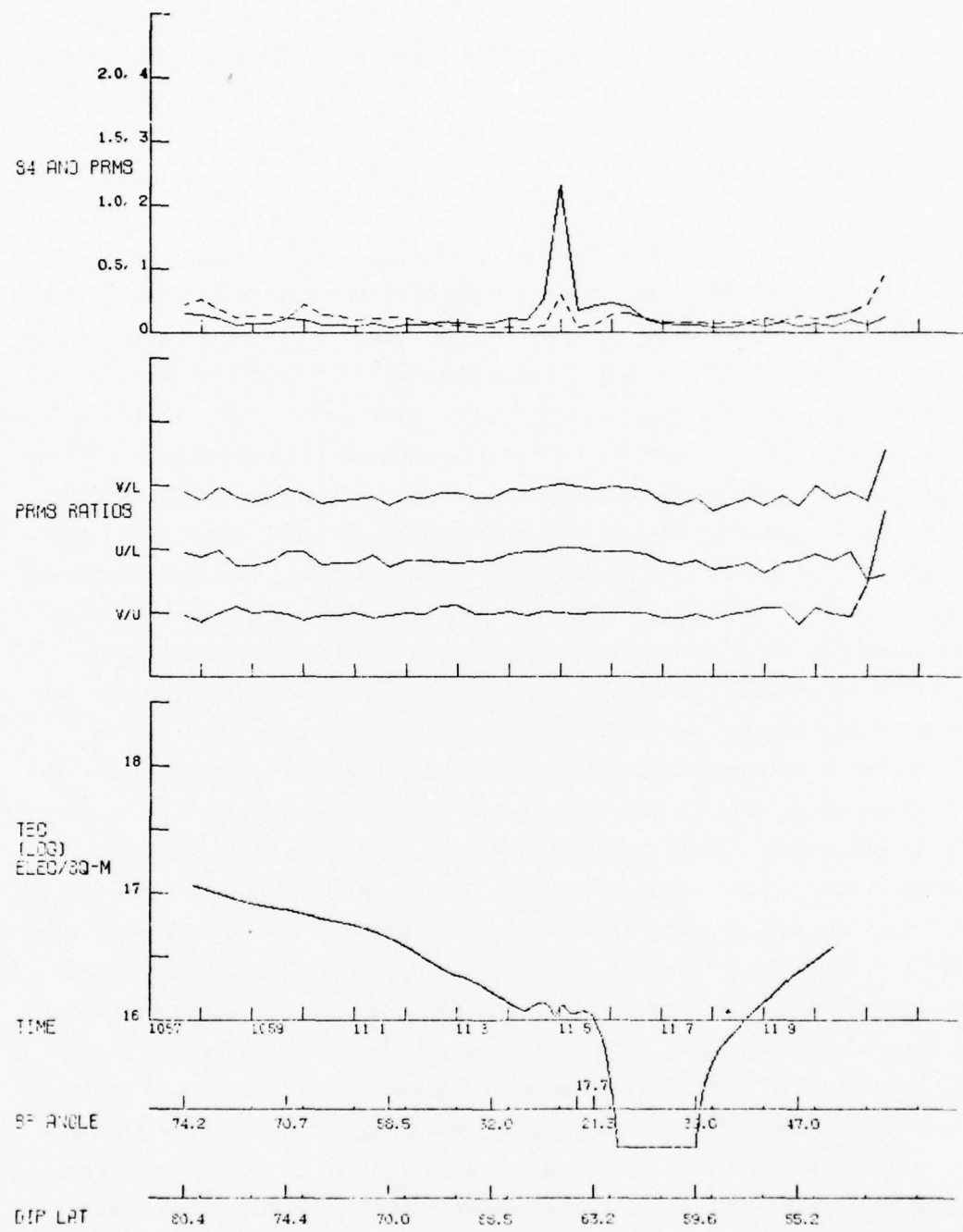


Figure 10: Scintillation records for WIDEBAND pass 7-2, 1105UT/8/6/76. The amplitude scintillations are denoted S4 (dashed lines) and the phase scintillations PRMS (solid lines). The center plot shows the ratios of VHF/UHF/L-BAND. The lower plot is of total (integrated) electron content.

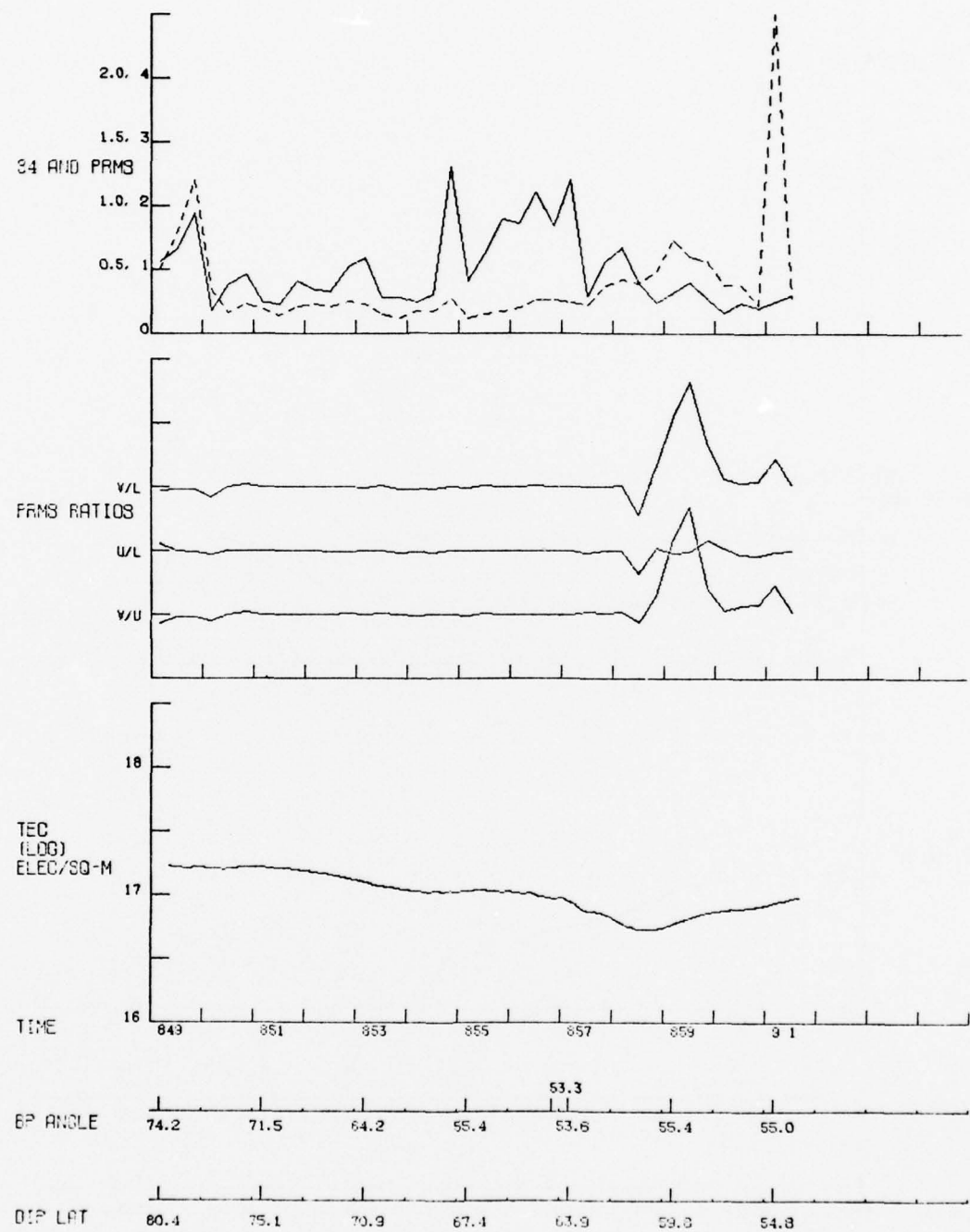


Figure 11. Scintillation records for WIDEBAND pass 5-37, 0855UT/6/6/76.

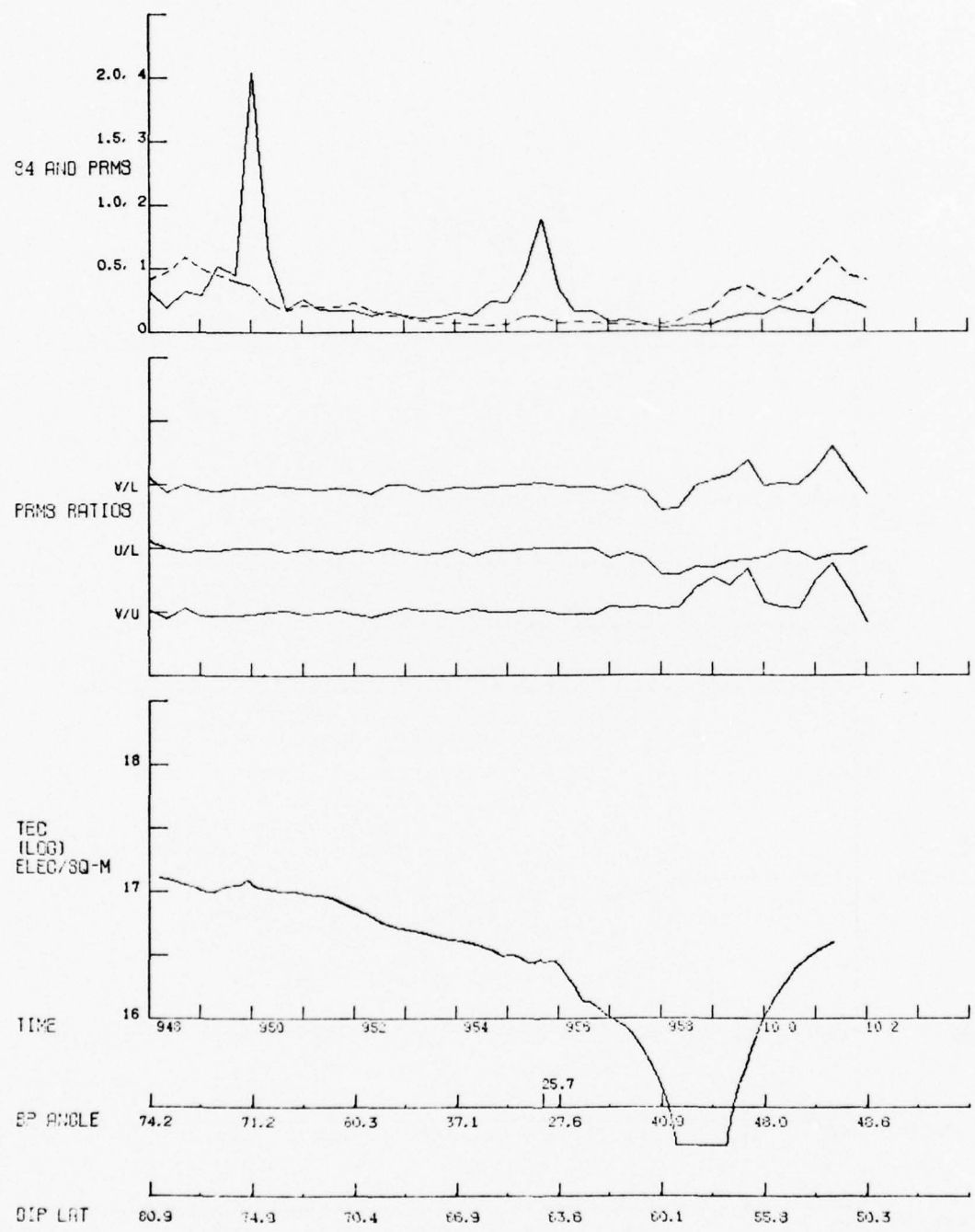


Figure 12. Scintillation records for WIDEBAND pass 6-47, 0955UT/7/30/76.

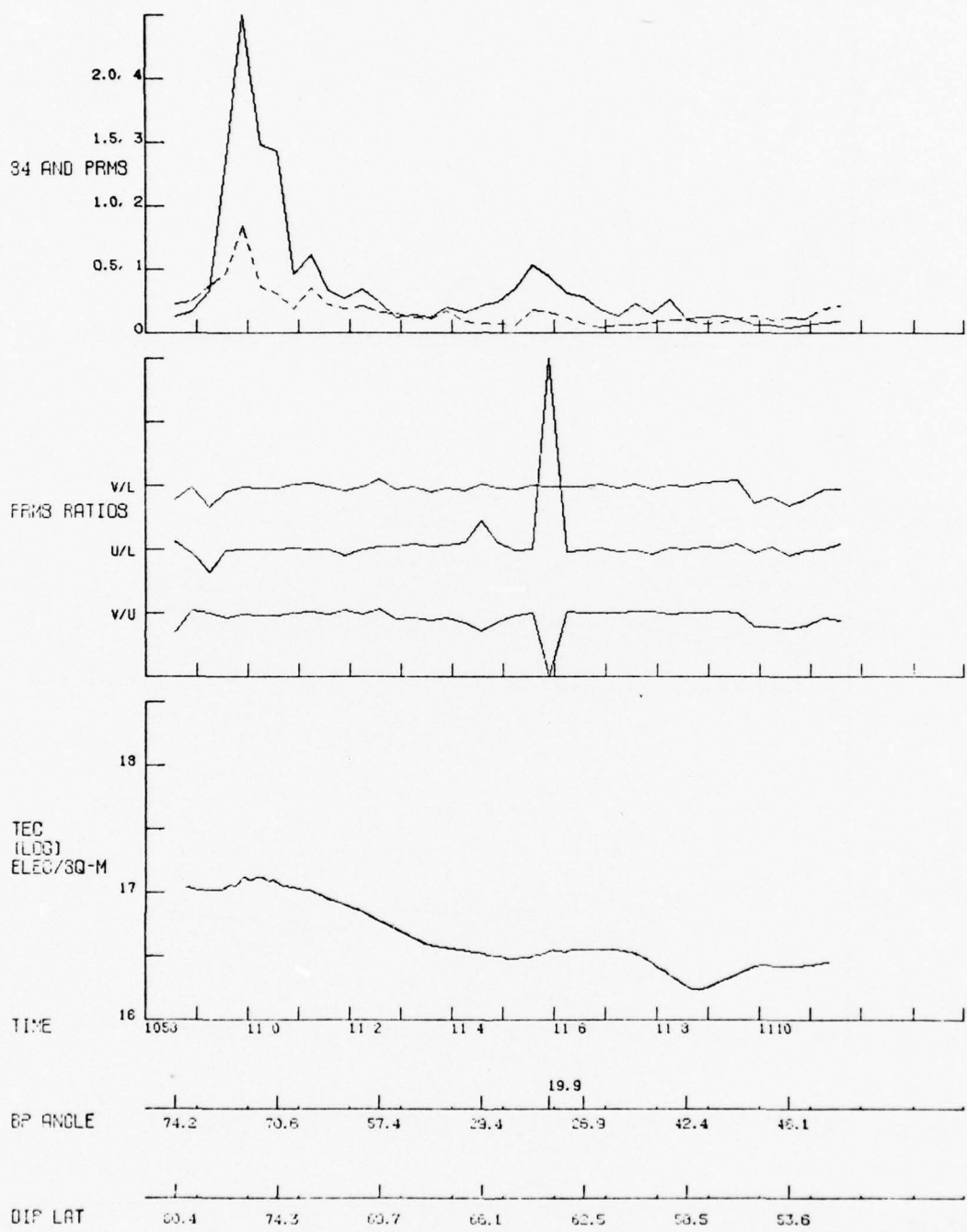


Figure 13. Scintillation records for WIDEBAND pass 5-36, 1105UT/6/4/76.

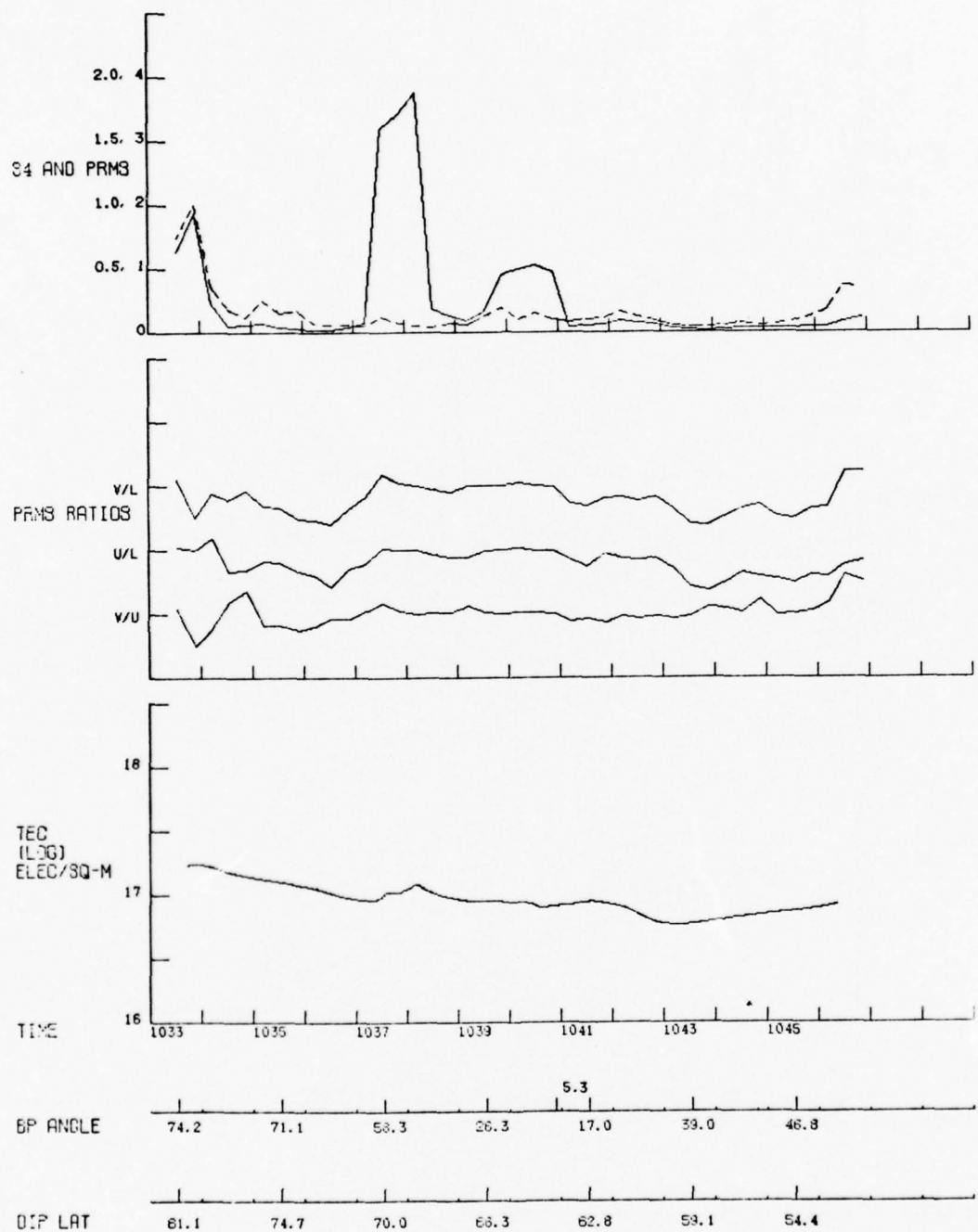


Figure 14. Scintillation records for WIDEBAND pass 5-38, 1040UT/6/6/76.

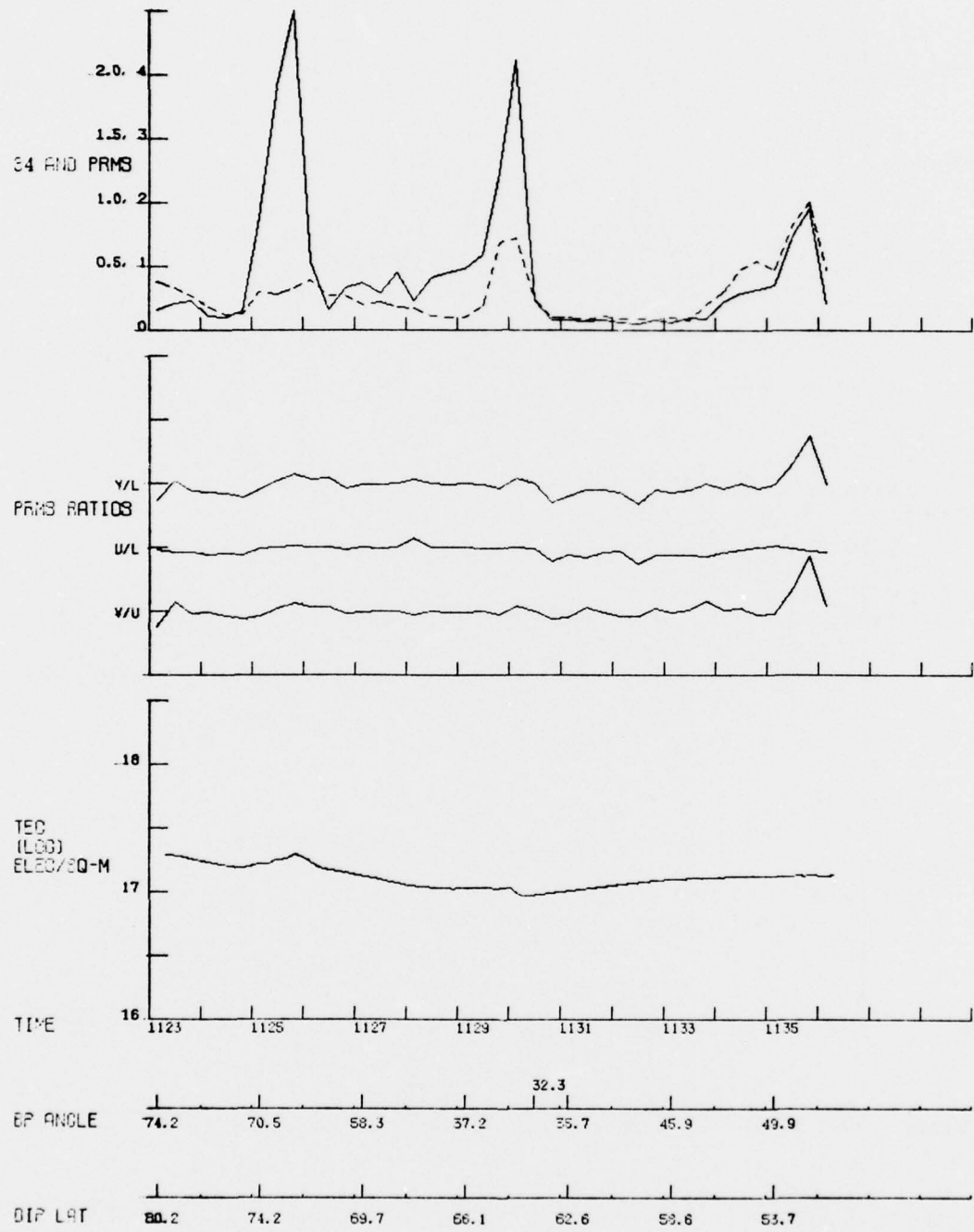


Figure 15. Scintillation records for WIDEBAND pass 6-8, 1130UT/6/23/76.

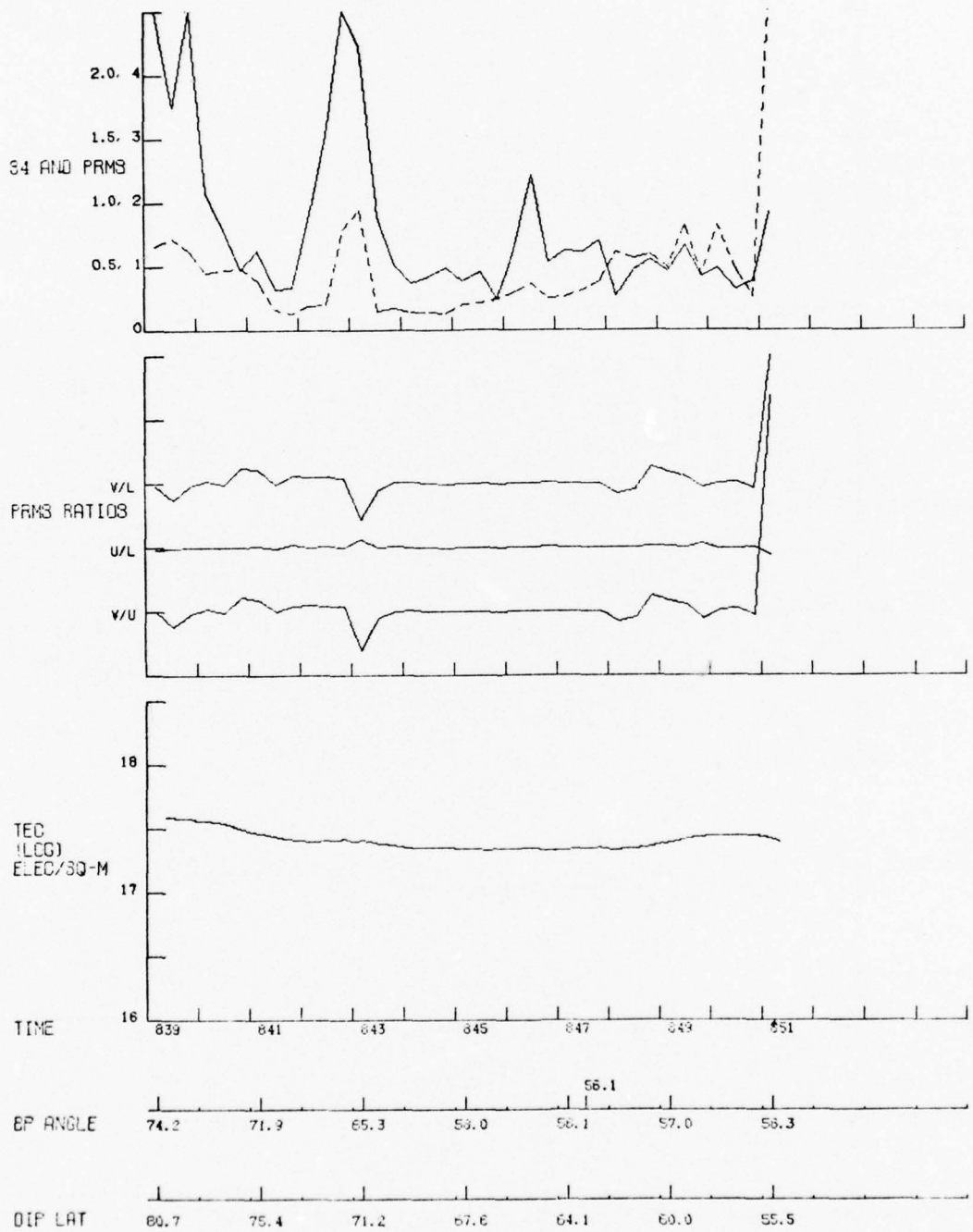


Figure 16. Scintillation records for WIDEBAND pass 5-50, 0835UT/6/11/76.

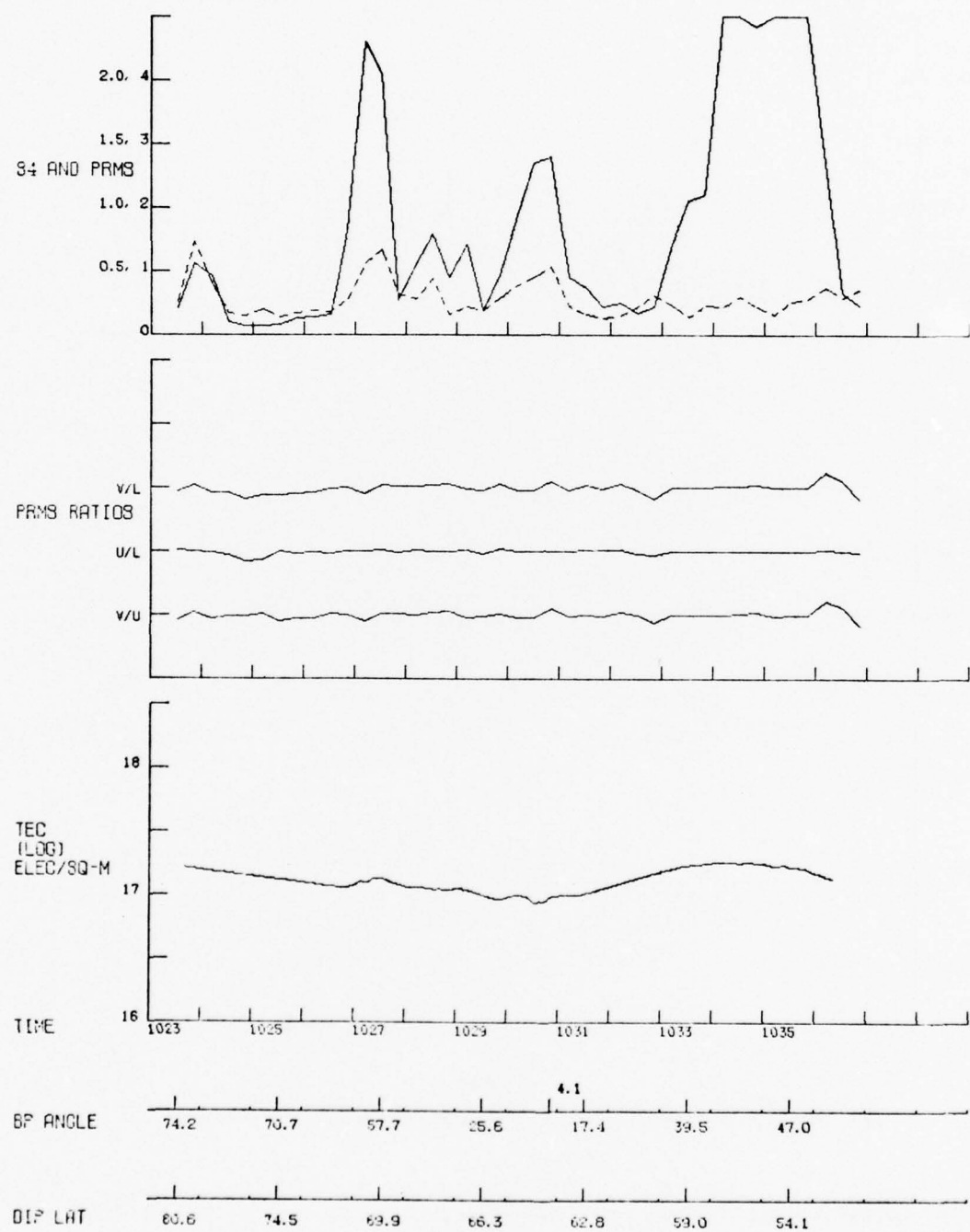


Figure 17. Scintillation records for WIDEBAND pass 5-51, 1030UT/6/11/76.

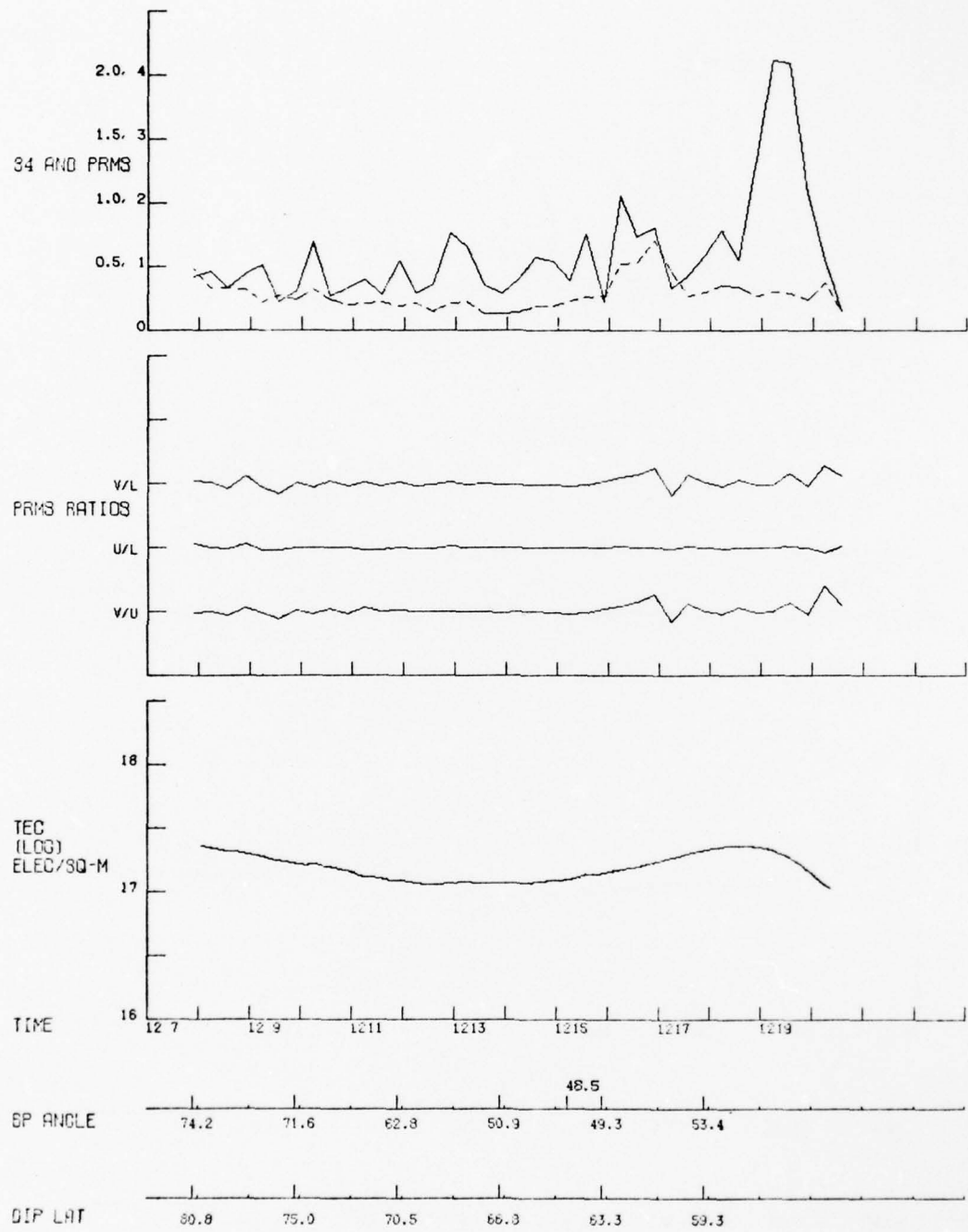


Figure 18. Scintillation records for WIDEBAND pass 5-52, 1115UT/6/11/76.

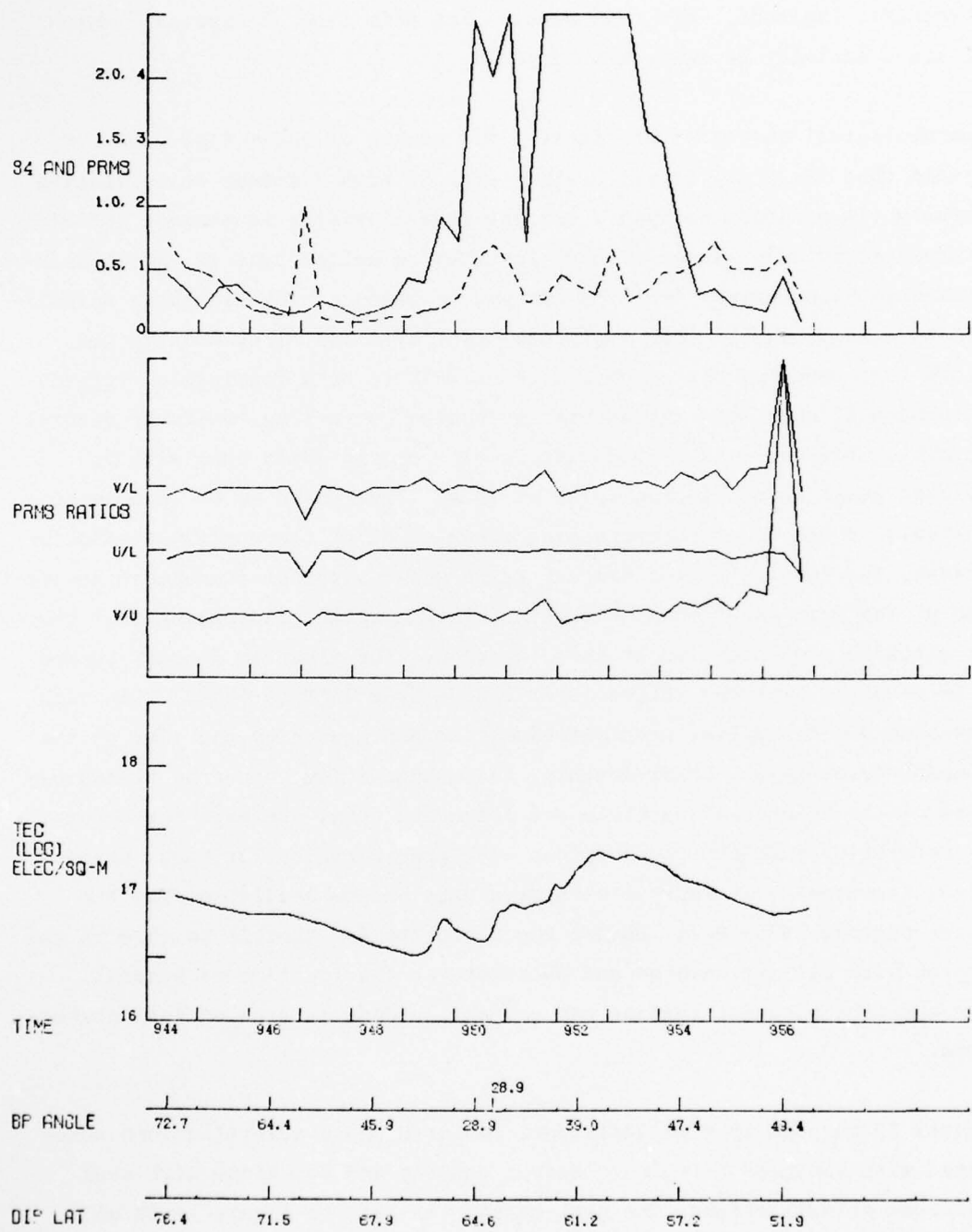


Figure 19. Scintillation records for WIDEBAND pass 7-42, 0950UT/9/2/76.

activity concentrated at its poleward edge. The phase and amplitude scintillation indices seem to follow the same trend, though the phase scintillations outweigh the amplitude scintillations between 64°N and 67°N geomagnetic latitude. For convenience, let this type of "typical" scintillation activity be designated Type I.

A morphological survey of the first 3-1/2 months of Poker Flat data reveals that there may be yet another type of high latitude scintillation activity (in addition to Type I and the characteristic equatorial and mid-latitude activity). These events, let them be called type II, are characterized as being mainly isolated patches or bands of intense phase scintillations accompanied by weak amplitude scintillations. They usually occur to the north edge of the auroral zone at 70°N to 80°N longitude. Figures 12 through 19 show some representative cases for varying levels of general activity. Figure 12 is a good example of a mostly quiet pass with an isolated phase scintillation spike at 75°N. (The spike at 64° should be ignored.) There is no corresponding enhancement of the amplitude scintillations. The total electron content trace shows a patch of enhanced ionization at the same location as the scintillation spike, indicating that there was particle precipitation at that location. The electron density seemed to be elevated over the entire auroral zone from 75°N to 64°N. This might have been due to earlier precipitation that had ceased by the time of the WIDEBAND observation. Unfortunately, this supposition cannot be tested because of the absence of particle precipitation data. Perhaps the chances of correlating WIDEBAND observations with precipitation (or known precipitation features) will improve when more data become available from the winter period, 1976-1977. During the winter it is feasible to observe the aurorae with all-sky cameras and photometers; the location of auroral arcs and precipitation regions can be readily deduced from optical observations.

Figures 13 through 15 show additional isolated phase scintillations associated with enhanced F-region electron density and sometimes with weak amplitude scintillations. The peak at the far left on Figure 14 is an instrumental effect and should be ignored.

Figure 16 is distinguished from the previous examples by the activity over the entire latitude range, and by the broad band of elevated total electron content. The plasma trough is not immediately discernible, but there seems to be a fall-off in TEC far to the right, as if the trough had been moved to $L \approx 3$. An examination of the geomagnetic indices for 0835 UT June 11, 1976, when the satellite was overhead, reveals that there was a major geomagnetic storm on that day with a sudden commencement at 0000 UT. This was one of the largest storms during the entire year; and by 0835 UT the DST value had reached -51, indicating that a fully-developed ring current had been established. The local time at Poker Flat is 10 hours earlier than UT, or 2235 LT. The WIDEBAND observations of Figure 16 were made just before local midnight, so it is reasonable to suppose that the scintillations at 79°N and 72°N were related to intense auroral arcs. The observations were made near midsummer so the auroral activity could not be observed against the brightly lit sky.

The succeeding WIDEBAND passes also furnished good data, shown in Figures 17 and 18. Figure 18 is for a pass near local midnight; overhead at 0030 LT. This time was coincident with the maximum D_{ST} of -61. The trough had moved to its southward limit, and the center of the scintillation activity had moved in to the edge of the trough. The very strong scintillations north of the trough are not of the expected Type I, but appear to be almost entirely phase scintillations. By the next pass, Figure 18, at 0215 LT the scintillation activity has decreased, though the phase scintillation component still dominates. The TEC curve has become smoother, indicating that the intense precipitation had subsided. But the tough, and the Type II scintillations at its edge, has only begun to move back, with the beginning of the recovery phase ($D_{ST} = -52$).

So far, efforts to correlate the Type II scintillation with S3-3 and other satellite data have been unsuccessful. There were several storms and geomagnetically active periods shortly after the S3-3 satellite was launched on July 15, 1976 but so far we have not found satisfactory coordinated passes. We have also looked at ephemerides of other satellites in the first four months of WIDEBAND operations and found no suitable coincidences.

3.4 MORPHOLOGY OF SCINTILLATIONS

That there exist several distinct types of high latitude scintillation activity is clear. It is tempting to associate the Type II events with auroral arcs and precipitation regions. The cases described are certainly in the expected locations. The associated TEC enhancements are suggestive but not conclusive. In the preceding figures the bumps in the TEC were small, and did not indicate large increases in the electron densities. Figure 19 perhaps illustrates the electron density increases more clearly. This remarkable pass also coincided with the main phase of a geomagnetic storm (0135 LT, Sept. 2, 1976, $D_{ST} = -31$). The TEC excursions here indicate order-of-magnitude increases in the electron density, again associated with high phase scintillation activity.

A more complete picture of the morphology of the scintillations is presented in Figure 20. Here only the widths of the rms phase scintillation peaks that exceeded 1 radian were plotted. Three degrees of shading are used to indicate levels of activity (these levels are not the same as the activity levels described in reference 17). No attempt was made to separate out the Type I activity from the Type II activity. Also shown is the location of the plasma trough, estimated from the TEC records. The pass numbers and overhead times are listed for all the WIDEBAND nighttime passes up to Sept 3, 1976. To the far right are listed several global geomagnetic indices. The daily sums of K_p are weighted toward the polar regions, and indicate the level of storm and substorm activity. The hourly D_{ST} records are weighted toward the equator, and are valuable for assessing the development of the ring current (at $L \sim 3-5$) during magnetic storms.

Several features stand out in Figure 20. The centers of scintillation activity and the plasma trough move northward and southward in response to geomagnetic activity. The storms of June 11, June 30, and Sept. 2 stand out especially. But the most striking aspect of the morphology is the regularity of the structures of roughly $1-2^\circ$ latitudinal extent. Translated into horizontal distance these structural features are of the order of 100 to 200 km wide. The structure is real; the spatial sampling rate is much smaller

THIS PAGE IS BEST QUALITY PRACTICABLE
FROM COPY FURNISHED TO DDC

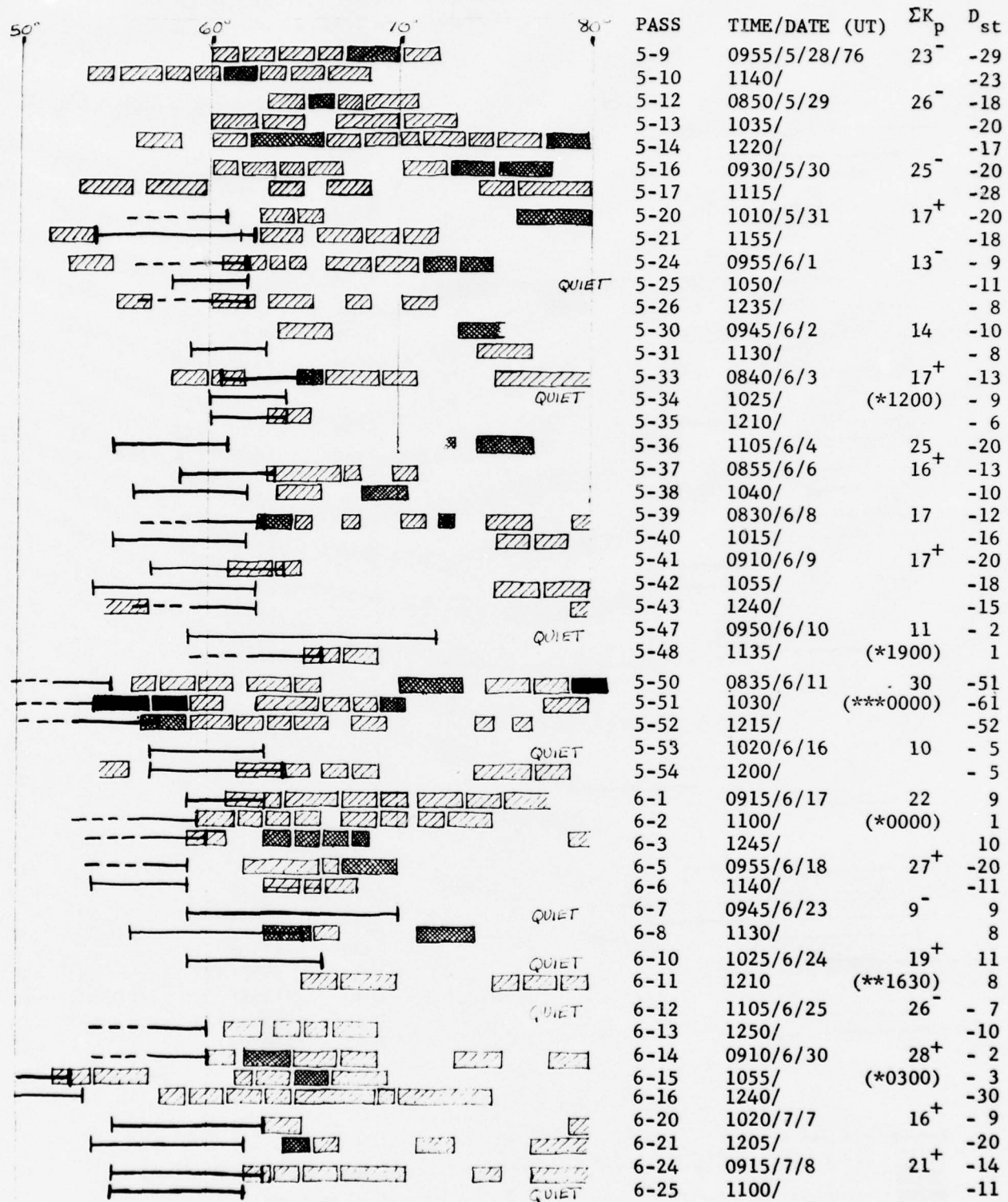
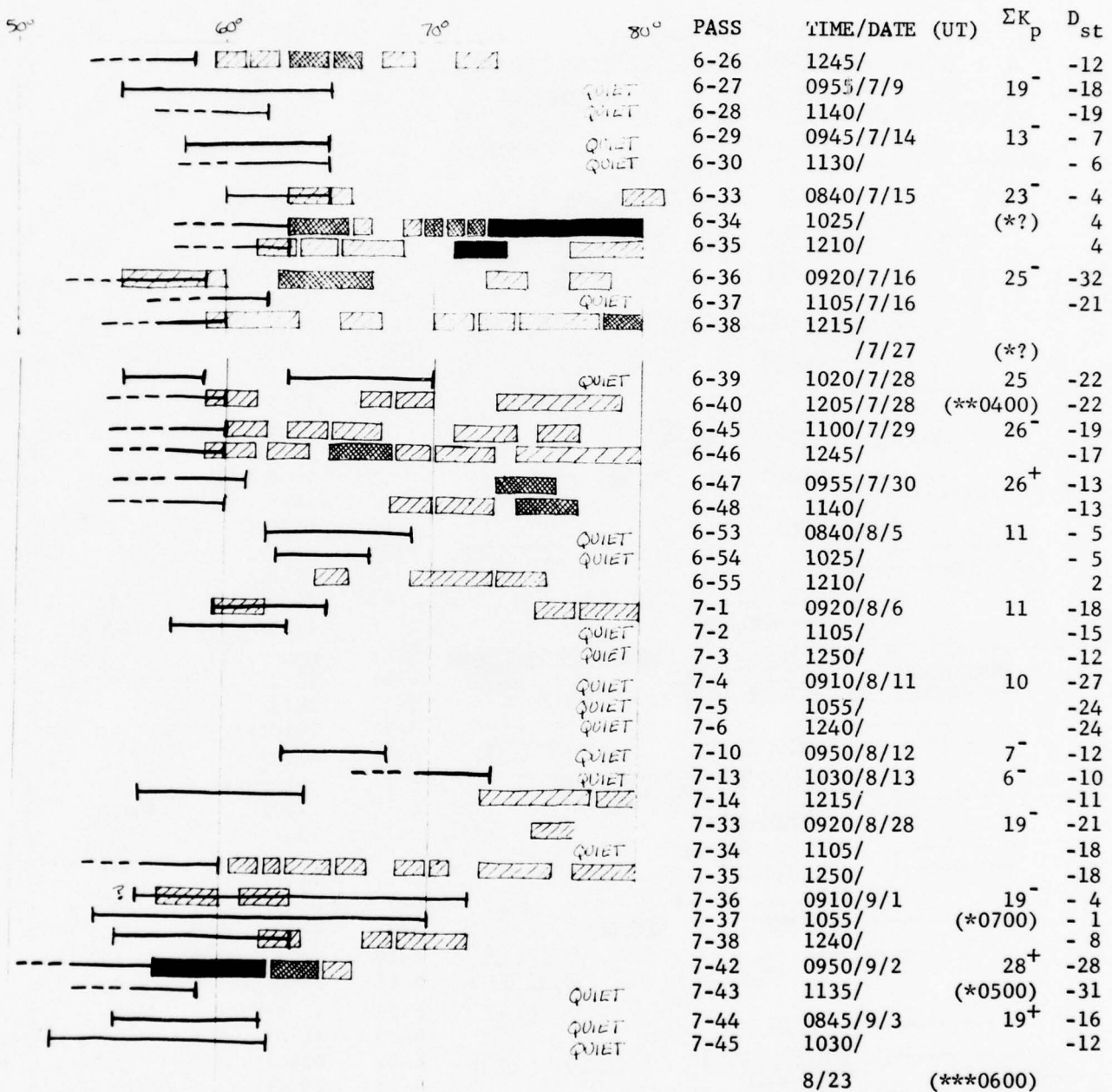


Figure 20a. The morphology of high-latitude WIDEBAND scintillation observations up to 9/3/76. The shaded bars are regions of intense phase scintillations. The location of the plasma trough (heavy solid line) is estimated from the total electron content as deduced from the WIDEBAND data.

THIS PAGE IS BEST QUALITY PRACTICABLE
FROM COPY FURNISHED TO DDC



PLASMA BREAK
 MODERATE OR INTENSE DISTURBANCES
 VERY INCREASE
 EXTREMELY INCREASE

* Note LT(Poker Flat)
= UT-1000

Figure 20b. The morphology of high-latitude WIDEBAND scintillation observations up to 9/3/76. (continued)

than the smallest structural features indicated on the figure. The structural patterns are consistent with their interpretation as auroral features. When the scintillation peaks are plotted, as here, the isolated peaks stand out quite clearly. Taken as a whole, the morphology of the scintillation regions very much resembles the morphology of precipitation events and aurorae in a meridian near local midnight.

3.5 DISCUSSION OF RESULTS

Our tentative interpretation of the Type II scintillations is that they are related to the large scale electric field structures discussed in the preceding sections. Their statistical occurrence is similar enough that more work should be done to find and interpret coordinated observations. The bodies of WIDEBAND and S3-3 data are large enough that good coordinated pass should be found in the later records that haven't yet been analyzed. It must be recognized, however, that a triple coordination is needed: between two satellites and an active region. Ideally, these questions could best be answered if a successor to the WIDEBAND satellite were put in orbit with on-board particle detectors that could delineate the precipitation features and the electric field structures.

Why the Type II scintillations should be associated with electron precipitation is not well understood. The scintillations are due mainly to processes in the F region, at altitudes near 300 km. The normal type of scintillation, presumably Type I, is expected to result from small scale field aligned irregularities formed by plasma instabilities. The classical example is in the equatorial electrojet, where streaming type instabilities cause the formation of field-aligned tubes with enhanced densities. The characteristics of the regions responsible for type II scintillations may become better known when some cases are examined in detail, to ascertain the statistics of the scintillation components [see ref. 17]. At the moment the only solid pieces of evidence are their size and occurrence, and the predominance of phase scintillations. All these characteristics tend to contradict the interpretation of Type II as being due to field-aligned plasma irregularities. One possible interpretation is that the

Type II scintillations result when the propagation path passes through the "pencils" of ionization caused by the precipitating electrons that are responsible for the fine scale auroral features. Optical observations have not set lower limits on the sizes of auroral forms, they might have sizes down to the gyroradii of the electrons. A 12 keV electron, for instance, has a gyroradius in the F-region of about 1 meter. This gives a scale size rather larger than the anticipated irregularities; somewhat smaller-scale irregularities with a fairly high degree of spatial organization would be needed to cause intense amplitude scintillations, especially in the UHF and higher frequencies.

Section 4
PLASMA IRREGULARITIES RESULTING FROM A H.A.N.E.

4.1 INTRODUCTION

A high-altitude nuclear explosion deposits considerable energy in the upper atmosphere and injects hot plasma into the magnetosphere. The configuration of the thermal plasma due to the enhanced ionization and heating of the atmosphere is unstable. It expands along the local magnetic field and breaks up into irregularities which have a broadband spatial structure. The gradient-drift instability appears to be the most important mechanism responsible for these irregularities, and much attention has been given to the assessment of effects due to this mechanism.

On the other hand, the hot plasma, i.e., the nuclear debris and the relativistic electrons, injected into the magnetosphere produces electric fields and currents which extend to thousands of kilometers both along and across magnetic field lines. These currents are susceptible to streaming instabilities which produce electrostatic waves and associated irregularities. The field-aligned currents can produce irregularities to altitudes of several thousand kilometers, as discussed in Section 2.1 (see Ref. 7); the cross-field currents produce the irregularities in the ionosphere, but they also propagate to high altitudes along the magnetic field (Ref. 20 and 21). All these irregularities resulting from the hot plasma extend to much greater distances than those due to the locally-heated atmosphere, but their duration may not be as long.

As discussed below, the injected-debris plasma produces both field-aligned and cross-field currents that may be unstable to the growth of electrostatic waves. The resulting irregularities are expected to occur northward of the burst to latitudes near the auroral zone. The relativistic electrons emitted by the fission debris are expected to produce only cross-field currents which may be unstable. However, owing to the eastward-drift motion of these electrons, the resulting irregularities are expected to occur over a considerable distance east of the burst meridian.

4.2 CURRENTS DUE TO INJECTED DEBRIS

A large fraction of the debris from a H.A.N.E. moves upward along the magnetic tube that is referred to as the debris tube. The energy of the ionized debris is high, and it therefore drifts rapidly toward the west owing to the configuration of the earth's magnetic field. On the other hand, the energetic electrons emitted by the debris drift toward the east. The resulting charge separation produces a large electric field across the tube, directed toward the east. This field causes the plasma in the tube to drift outward ($\bar{E} \times \bar{B}$ direction) toward higher L values. Simultaneously, thermal plasma currents flow along the magnetic field lines containing the excess charges and across magnetic field lines in the ionosphere tending to neutralize the excess charges.

In an investigation of the debris motion (Ref. 22) it was found that for bursts in the megaton range the excess charges are never fully neutralized. Hence, the debris tube continues to drift outward to the limit of the trapping region of the magnetosphere. Moreover, the investigation reveals that the field-aligned currents exceeded the instability threshold value which was given by Kindel and Kennel (Ref. 7) and verified by the S3-3 satellite data (Ref. 3). Plasma irregularities similar to those observed with the S3-3 satellite - extending to altitudes in excess of about 8000 km - should therefore be expected along all "closed" field lines north of the burst.

The electric field across the tube also appears in the E-region of the ionosphere. There, the electrons drift essentially according to the $\bar{E} \times \bar{B}$ drift velocity, but the ions are greatly restricted by collisions with the neutral constituents of the atmosphere. Hence, the relative drift velocity of the electrons with respect to the ions depends on the magnitude of the electric field. According to the Farley-Buneman criterion, the resulting ionospheric current becomes unstable if the relative electron-ion drift velocity exceeds the thermal velocity of the ions.

Using the model for the debris-tube motion described in Ref. (22), the electric field in the ionosphere was computed for the parameters of Starfish and the USSR burst of Oct. 22, 1962. The thermal velocities of the ions were computed assuming that they were in thermal equilibrium with the neutral atmosphere in the E-region. It was found that the $\bar{E} \times \bar{B}$ drift velocity of the electrons exceeded 10^5 m/sec at latitudes higher than 19°N in the case of Starfish. For the USSR burst, the drift velocity exceeded 10^5 m/sec at latitudes above 41°N . The relative drift velocity, therefore, far exceeded the ion thermal velocities, which were found to be in the range 420-480 m/sec, depending on diurnal and solar-activity conditions. Hence, as stated above, plasma irregularities following a high-yield burst should be expected from the ionosphere to altitudes of 8000 km or more on field lines extending from the burst point to the auroral zone.

4.3 CURRENTS DUE TO INJECTED ELECTRONS

As the debris tube drifts outward, the electrons emitted by the debris continually drift out of the tube toward the east. Owing to velocity dispersion the electron distribution spreads toward the east and large-scale electric fields ensue from the excess charges. Again, thermal-plasma currents along magnetic field lines tend to neutralize the excess charges but these charges cannot be neutralized in times less than the time required for a hydromagnetic wave to traverse a field line. During that time the distribution of the injected electrons changes as the electrons drift across magnetic field lines toward the east; thus, the electric field persists while the electrons remain bunched during their drift motion.

In a model discussed in Ref. (22), the electric field across the magnetic field due to the injected electrons was computed, taking into account the effects of the changing injected-electron distribution and the neutralizing currents. The field was computed for the electrons injected by Starfish and the USSR test of Oct. 22, 1962. Again, this field was transformed

to the E-region of the ionosphere, and the resulting $\bar{E} \times \bar{B}$ drift velocity of the electrons was determined. It was found that, for the Starfish distribution, the relative drift velocity of the electrons with respect to the ions exceeded the thermal velocity of the ions in the latitude range $20\text{--}56^\circ\text{N}$ and in a longitudinal interval extending from the burst meridian to about 60°E . For the USSR burst, the relative drift velocity exceeded the ion thermal velocity at latitudes between 41°N and 51°N , and at longitudes extending to about 40° east of the burst meridian.

The field-aligned currents due to the injected electrons did not exceed the Kindel and Kennel instability criterion. Hence, only the ionospheric irregularities should be expected over the regions given above.

The duration of the irregularities is uncertain. It is likely that they will persist at least as long as the driving perturbation remains. For the case of the debris motion, the perturbation may last only a few hundred seconds. For the case of the injected electrons, it lasts about 1/2 hour at $L \approx 2$. However, the duration of the electric field is proportional to the longitudinal drift period of the electrons. Hence, since the drift period is inversely proportional to L , the duration of the perturbation should decrease toward higher L values.

Section 5
REFERENCES

1. Cladis, J. B., G. T. Davidson, W. E. Francis, L. L. Newkirk, and M. Walt, "Investigation of Ionospheric Disturbances," Final Report, DNA 4225F, 28 January 1977.
2. Kintner, P., M. C. Kelley, F. S. Mozer, and R. Torbert, "Electrostatic Ion Cyclotron Waves at High Altitudes in the Auroral Oval and their Relation to Paired Electrostatic Shocks," EOS 58, 473, 1977.
3. Mozer, F. S., C. W. Carlson, M. K. Hudson, R. B. Torbert, B. Parady, J. Yatteau, and M. C. Kelley, "Observations of Paired Electrostatic Shocks in the Polar Magnetosphere," Phys. Rev. Lett., 38, 292, 1977.
4. Shelley, E. G., R. D. Sharp, and R. G. Johnson, "Satellite Observations of an Ionospheric Acceleration Mechanism," Geophys. Res. Letters, 3, 654, 1976.
5. Hudson, M. K., R. L. Lysak, and F. S. Mozer, "Magnetic Field Aligned Potential Drops Due to Electrostatic Ion Cyclotron Turbulence," Preprint, University of California, Berkeley, June, 1977.
6. Fälthammar, C.-G., "Generation Mechanisms for Magnetic-Field-Aligned Electric Fields in the Magnetosphere," Preprint TRITA-EPP-77-21, Dept. of Plasma Physics, Royal Inst. of Technology, 100 44 Stockholm, Sweden, 1977.
7. Kindel, J. M., and C. F. Kennel, "Topside Current Instabilities," J. Geophys. Res., 76, 3055, 1971.
8. Gurnett, P. A., and L. A. Frank, "A Region of Intense Plasma Wave Turbulence on Auroral Field Lines," University of Iowa Report 76-12, 1976.
9. Block, L. P. and C.-G. Fälthammar, "Mechanisms that may Support Magnetic-Field-Aligned Electric Fields in the Magnetosphere," Ann. Geophys., 32, 161, 1976
10. Swift, D. W., "On the Formation of Auroral Arcs and Acceleration of Auroral Electrons," J. Geophys. Res., 80, 2096, 1977.
11. Frank, L. A., and K. L. Ackerson, "Observations of Charged Particle Precipitation into the Auroral Zone," J. Geophys. Res., 76, 3612,

12. Ghielmetti, A., R. G. Johnson, E. G. Shelley, and R. D. Sharp, "Average Properties of Upstreaming Energetic Field Aligned Ions," EOS 58, 1211, 1977.
13. Ghielmetti, A., R. G. Johnson, E. G. Shelley, and R. D. Sharp, "Angular Distribution Characteristics of Up-Streaming Energetic (keV) O⁺ and H⁺ ions, EOS, 58, 473, 1977.
14. Fennell, J. F., Private Communication, 1977.
15. Persson, H., "Electric Field Along a Magnetic Line of Force in a Low-Density Plasma," Phys. Fluids, 6, 1756, 1963.
16. Mozer, F. S., private communication, 1977.
17. Fremouw, E. J., Examination of Data from the WIDEBAND Satellite Experiment, Interim Progress Report, Contract 14237, Physical Dynamics, Inc., Seattle, Wash., August, 1977.
18. Sears, R. D., Ionospheric Irregularities: Optical Support of HAES Scintillation Experiments, DNA 4240F, January 1977
19. Vampola, A. L., and G. A. Kuck, Induced Precipitation of Inner Zone Electrons 1: Observations, SAMSO TR-77-134, July 1977.
20. Buneman, O., "Dissipation of Currents in Ionized Media," Phys. Rev., 115, 503, 1959.
21. Farley, D. T., Jr., "A Plasma Instability Resulting in Field-Aligned Irregularities in the Ionosphere," J. Geophys. Res. 68, 6083, 1963.
22. Cladis, J. B., Davidson, W. E. Francis, and L. L. Newkirk, Task Report on New Electron Injection Model, AFWL Contract F29601-76-C-0095, LMSC/D567089, September 30, 1977.

DISTRIBUTION LIST

DEPARTMENT OF DEFENSE

Director
 Command Control Technical Center
 ATTN: C-650, W. Heidig

Director
 Defense Advanced Rsch. Proj. Agency
 ATTN: Strategic Tech. Office
 ATTN: Nuclear Monitoring Research

Defense Communication Engineer Center
 ATTN: Code 700, J. Lebo
 ATTN: Code R 103, D. T. Worthington
 ATTN: Code R 720, John Worthington
 ATTN: Code R 103, J. Raffensberger

Director
 Defense Communications Agency
 ATTN: Code 810, R. W. Rostron

Defense Documentation Center
 Cameron Station
 12 cy ATTN: TC

Director
 Defense Intelligence Agency
 ATTN: DI-7D
 ATTN: DT-1C
 ATTN: DT-1, Mr. Knoll

Director
 Defense Nuclear Agency
 ATTN: TISI Archives
 ATTN: RAAE, Maj. R. Bigoni
 ATTN: DDST
 ATTN: RAEV
 ATTN: STVL, E. Lavier
 2 cy ATTN: RAAE, Charles A. Blank
 3 cy ATTN: TITL, Tech. Library

Commander, Field Command
 Defense Nuclear Agency
 ATTN: FCPR

Director
 Interservice Nuclear Weapons School
 ATTN: Doc. Con.

Director
 Joint Strat. Tgt. Planning Staff
 ATTN: Doc. Con.

Chief
 Livermore Division, Field Command, DNA
 Lawrence Livermore Laboratory
 ATTN: FCPRL

Director
 National Security Agency
 ATTN: Tech. Library
 ATTN: TDL

OJCS/J-3
 ATTN: WWMCCS, Eval. Ofc., Mr. Toma
 ATTN: J-3 Environmental Services Div.

DEPARTMENT OF DEFENSE (Continued)

OJCS/J-5
 ATTN: Nuclear Division

Under Secretary of Def. for Rsch. & Engrg.
 ATTN: S&SS (OS)

DEPARTMENT OF THE ARMY

Commander/Director
 Atmospheric Sciences Laboratory
 U.S. Army Electronics Command
 ATTN: H. Ballard
 ATTN: E. Butterfield, DRSEL-BL-SY-R
 ATTN: R. Olsen
 ATTN: Robert Rubio
 ATTN: F. E. Niles, DELAS-AE-M

Director
 BMD Advanced Tech. Ctr.
 Huntsville Office
 ATTN: ATC, W. Davies
 ATTN: ATC-T, Melvin T. Capps

Program Manager
 BMD Program Office
 ATTN: DACS-BMT, John Shea

Commander
 BMD System Command
 ATTN: BDMSC-TEN, Noah J. Hurst

Dep. Chief of Staff for Rsch. Dev. & Acq.
 ATTN: DAMA-WSZ-C
 ATTN: DAMA-CSZ-C

Chief of Engineers
 ATTN: Fernand De Percin

Deputy Chief of Staff for Ops. & Plans
 ATTN: DAMO-SSN
 ATTN: DAMO-DDC, Col. D. W. Einsel

Commander
 Harry Diamond Laboratories
 ATTN: DELHD-NP, Francis N. Wimenitz

Director
 U.S. Army Ballistic Research Labs.
 ATTN: J. Heimerl
 ATTN: John G. Mester
 ATTN: Tech. Lib., Edward Baicy

Commander
 U.S. Army Electronics Command
 ATTN: DRSEL-XL-D
 ATTN: DRSEL-RD-P
 ATTN: DRSEL-TL-IR, Edwin T. Hunter
 ATTN: DRSEL-PL-ENV, Hans A. Bomke
 ATTN: Stanley Kronenberg

Commander
 U.S. Army Foreign Science & Tech. Ctr.
 ATTN: R. Jones

DEPARTMENT OF THE ARMY (Continued)

Commander
 U.S. Army Materiel Dev. & Readiness Cmd.
 ATTN: DRCLDC, J. A. Bender
 ATTN: DRXCD-TL

Commander
 U.S. Army Missile Command
 ATTN: DRDMI-XS, Chief Scientist
 ATTN: DRSMI-ABL

Commander
 U.S. Army Nuclear & Chemical Agency
 ATTN: Library

Commander
 U.S. Army Satcom Agency
 ATTN: Tech. Lib.

Chief
 U.S. Army Research Office
 ATTN: CRDARD-P, Robert Mace
 ATTN: CRDARD-DCS, Hermann R. Robl

Commander
 Whippany Field Office (BMDSC-WS-W)
 Bell Telephone Laboratories
 ATTN: John Turner

Commander
 White Sands Missile Range
 ATTN: Willis W. Webb, AMSEL-NL-SD
 ATTN: Marvin P. Squires, STEWS-TE-NT

DEPARTMENT OF THE NAVY

Chief of Naval Operations
 ATTN: Code 604C3, Robert Piacesi
 ATTN: Op 981

Chief of Naval Research
 ATTN: Code 461, R. Gracen Joiner
 ATTN: Code 461, Jacob L. Warner

Commander
 Naval Electronic Systems Command
 Naval Electronic Systems Cmd. Hqs.
 ATTN: PME 117-T, Satellite Comm. Proj. Off.
 ATTN: ELEX 03

Commanding Officer
 Naval Intelligence Support Ctr.
 ATTN: Doc. Con.
 ATTN: Code 40A, E. Blase

Commander
 Naval Ocean Systems Center
 ATTN: Code 2200, Ilan Rothmuller
 ATTN: Tech. Lib. for T. J. Keary
 ATTN: Code 532, William F. Moler
 ATTN: Code 2200, Jurgen Richter
 ATTN: Code 2200, Richard Pappert

Superintendent (Code 1424)
 Naval Postgraduate School
 ATTN: Code 61 DY, J. N. Dyer
 ATTN: Code 61 MN, E. A. Milne
 ATTN: Code 2124, Tech. Rpts. Librarian

DEPARTMENT OF THE NAVY (Continued)

Director
 Naval Research Laboratory
 ATTN: Code 2600, Tech. Lib.
 ATTN: Code 6750, Darrell F. Strobel
 ATTN: Code 7125.7, Donald J. Horan
 ATTN: Code 7709, Wahab Ali
 ATTN: Code 7128, James D. Kurfess
 ATTN: Code 6701, Jack D. Brown
 ATTN: W. Neil Johnson
 ATTN: Code 6750, S. L. Ossakow
 ATTN: Code 7127, Charles Y. Johnson
 ATTN: Code 6750, Klaus Hain
 ATTN: Code 7120, Gerald H. Share
 ATTN: Code 7120, Robert L. Kinzer
 ATTN: Code 6461, Francis J. Campbell
 ATTN: Code 4104, Emanuel L. Brancato
 ATTN: Code 5174, Frederick W. Raymond
 ATTN: Code 6623, Richard L. Statler
 ATTN: Code 6750, J. Davis
 ATTN: Code 6750, J. Fedder
 ATTN: Code 6700, Timothy P. Coffey

Officer-in-Charge
 Naval Surface Weapons Center
 ATTN: Code WA501, Navy Nuc. Prgms. Off.
 ATTN: D. L. Land
 ATTN: L. Rudlin

Commanding Officer
 Naval Astronautics Group
 6 cy ATTN: W. J. Gleason

Commanding Officer
 Nuclear Weapons Tng. Center, Pacific
 ATTN: Nuclear Warfare Department

Commander
 Nuclear Weapons Tng. Group, Atlantic
 ATTN: Nuclear Warfare Department

DEPARTMENT OF THE AIR FORCE

Commander
 ADC/DO
 ATTN: DOF
 ATTN: DOFS
 ATTN: DOA

Commander
 ADCOM/XPD
 ATTN: Hqs. 14th Aerospace Force (Evn.)
 ATTN: XPQDQ
 ATTN: XPQDQ, Maj G. Kuch

AF Weapons Laboratory, AFSC
 ATTN: CC, Col G. J. Freyer
 ATTN: CA, Arthur H. Guenther
 ATTN: SUL
 ATTN: DYT, Capt Hollars
 ATTN: DYT, Joseph Janni
 ATTN: DYT, Capt Gary D. Cable

AFTAC
 ATTN: TN
 ATTN: TF/Maj Wiley
 ATTN: Tech. Lib.
 ATTN: TN-E, LtCol E. C. Thomas

DEPARTMENT OF THE AIR FORCE (Continued)

AF Geophysics Laboratory, AFSC

ATTN: LKB, A. Faire
ATTN: LKS, R. A. Van Tassel
ATTN: C. Stergis
ATTN: LKB, Kenneth S. W. Champion
ATTN: L. Katz
ATTN: PHG, J. C. McClay
ATTN: OPR-1, James C. Ulwick
ATTN: LKB, F. B. Innes
ATTN: LKB, T. J. Keneshea
ATTN: LKB, William Swider, Jr.
ATTN: LKD, Rocco S. Narcisi
ATTN: OPR, T. Connolly
ATTN: OPR, F. Billingsly
ATTN: LKO, Robert E. Huffman
ATTN: OP, John S. Garing
ATTN: OPR, Alva T. Stair
ATTN: OPR, R. O'Neill
ATTN: OPR, F. Delgreco
ATTN: OPR, Harold Gardner
ATTN: OPR, J. Kennealy
ATTN: OPR, R. E. Murphy
ATTN: SUOLA, E. L. Cunha

Headquarters

Air Force Systems Command
ATTN: DLXP, Capt Roisel
ATTN: DLS

Headquarters

Electronic Systems Division, (AFSC)
ATTN: W. C. Morton

Commander

Foreign Technology Division, AFSC
ATTN: TDPSS, Kenneth N. Williams
ATTN: NICD, Library
ATTN: WE

Hq. USAF/IN

ATTN: IN

Hq. USAF/RD

ATTN: RDPM
ATTN: RDSA
ATTN: RDQSM
ATTN: RD
ATTN: RDPS

Commander

Rome Air Development Center, AFSC
ATTN: V. Coyne, OCSE
ATTN: J. J. Simons, OCSE
ATTN: Doc. Library, EMTLD

SAMSO/DY

ATTN: DYE, LtCol W. E. Herdrich

SAMSO/SZ

ATTN: SZJ, Major Lawrence Doan

Commander in Chief

Strategic Air Command
ATTN: XPFS, Maj Brian G. Stephan

USAFETAC/CB

ATTN: CBT, Mr. Creasi

DEPARTMENT OF THE AIR FORCE (Continued)

Commander

ASD
ATTN: ASD-XH-EX, LtCol Robert Leverette

Det. 1, IZWS

Space Forecasting Section
ATTN: R. M. Heslin

DEPARTMENT OF ENERGY

Department of Energy

Division of Headquarters Services

ATTN: Doc. Con. for H. H. Kurzweg
ATTN: Doc. Con. for George L. Rogosa
ATTN: Doc. Con. for Joseph D. Lafleur
ATTN: Doc. Con. for D. Kohlstad
ATTN: Doc. Con. for Richard J. Kandel
ATTN: Doc. Con. for Reports
ATTN: Doc. Con. for Class Tech. Lib.

Division of Military Application

ATTN: Doc. Con. for Frank A. Ross
ATTN: Doc. Con. for Maj D. A. Haycock
ATTN: Doc. Con. for Col T. Gross
ATTN: Doc. Con. for David H. Slade

University of California

Lawrence Livermore Laboratory
ATTN: J. F. Tinney, L-517
ATTN: Tech. Info., Dept. L-3

Los Alamos Scientific Laboratory

ATTN: Doc. Con. for W. M. Hughes, MS 559
ATTN: Doc. Con. for Donald Kerr
ATTN: Doc. Con. for R. A. Jeffries
ATTN: Doc. Con. for S. Rockwood
ATTN: Doc. Con. for John Zinn
ATTN: Doc. Con. for William Maier
ATTN: Doc. Con. for W. D. Barfield
ATTN: Doc. Con. for David W. Steinhaus
ATTN: Doc. Con. for E. A. Bryant
ATTN: Doc. Con. for E. W. Hones, Jr.
ATTN: Doc. Con. for Marge Johnson
ATTN: Doc. Con. for J. Judd
ATTN: D. M. Rohrer, MS 518
ATTN: Doc. Con. for John S. Malik
ATTN: Doc. Con. for Martin Tierney, J-10

Sandia Laboratories

Livermore Laboratory
ATTN: Doc. Con. for Thomas B. Cook, Org. 8000

Sandia Laboratories

ATTN: Doc. Con. for J. C. Eckhardt, Org. 1250
ATTN: Doc. Con. for Morgan L. Kramm, Org. 5720
ATTN: Doc. Con. for Frank P. Hudson, Org. 1722
ATTN: Doc. Con. for 3141, Sandia Rpt. Coll.
ATTN: Doc. Con. for Clarence R. Mehl, Org. 5230
ATTN: Doc. Con. for Org. 9220

OTHER GOVERNMENT AGENCIES

Central Intelligence Agency

ATTN: RD/SI, Rm. 5G48, Hq. Bldg. for
NED/OSI - 2G48, Hqs.

Department of Commerce

Office of Telecommunications
ATTN: William F. Utlauf

OTHER GOVERNMENT AGENCIES (Continued)

Department of Commerce
National Bureau of Standards
ATTN: M. Krauss
ATTN: M. Scheer
ATTN: Office of Director
ATTN: Lewis H. Gevantman
ATTN: K. Keesler
ATTN: B. Stiner
ATTN: J. Cooper
ATTN: D. Garvin
ATTN: D. R. Lide
ATTN: George A. Sinnatt

NASA
Goddard Space Flight Center
ATTN: J. Siry
ATTN: S. J. Bauer
ATTN: A. C. Aiken
ATTN: James I. Vette
ATTN: Gilbert D. Meade, Code 641
ATTN: A. Tempkin
ATTN: G. Levin
ATTN: Technical Library
ATTN: J. P. Hepner
ATTN: R. F. Benson
ATTN: H. A. Taylor
ATTN: M. Sugiura

NASA
George C. Marshall Space Flight Center
ATTN: R. Chappell
ATTN: W. T. Roberts
ATTN: C. R. Balcher
ATTN: W. A. Oran
ATTN: N. H. Stone
ATTN: R. D. Hudson

NASA
ATTN: R. Fellows
ATTN: P. Eaton
ATTN: E. R. Schmerling
ATTN: J. Naugle
ATTN: Code ST, D. R. William
ATTN: M. Tepper
ATTN: A. Schardt
ATTN: D. P. Cauffman
ATTN: G. Sharp
ATTN: J. Findlay
ATTN: R. A. Schiffer
ATTN: Code ST, W. L. Taylor

NASA
Johnson Space Center
ATTN: Owen Garriot
ATTN: Classified Lib., Code BM6

NASA
Ames Research Center
ATTN: N-245-3, Palmer Dyal
ATTN: M-254-4, R. Whitten
ATTN: C. P. Sonett
ATTN: N-245-4, Ilia G. Popoff

NASA Scientific & Technical Info. Fac.
ATTN: SAR/DLA-385
ATTN: Acq. Branch

OTHER GOVERNMENT AGENCIES (Continued)

National Oceanic & Atmospheric Admin.
National Weather Service
ATTN: L. Machta
ATTN: J. K. Angell

National Oceanic & Atmospheric Admin.
National Ocean Survey
ATTN: Gerald A. Peterson
ATTN: Edward S. Epstein
ATTN: Ronald L. Lavoie
ATTN: Wayne McGovern
ATTN: John W. Townsend, Jr.

National Oceanic & Atmospheric Admin.
Environmental Research Laboratories
ATTN: R43, Herbert H. Sauer
ATTN: R43, Donald J. Williams
ATTN: RXI, Robert W. Knecht
ATTN: George C. Reid, Aeronomy Lab.
ATTN: Eldon Ferguson
ATTN: A. H. Snailey
ATTN: Walther N. Spjeldvik
ATTN: Robert B. Doeker

National Science Foundation
ATTN: R. Manka
ATTN: W. H. Cramer
ATTN: F. Gilman Blake
ATTN: W. D. Adams
ATTN: E. P. Todd
ATTN: Rolf Sinclair
ATTN: Fred D. White
ATTN: M. K. Wilson
ATTN: R. S. Zapolsky

U.S. Arms Control & Disarmament Agcy.
ATTN: Office of Director
ATTN: Reference Info. Center

DEPARTMENT OF DEFENSE CONTRACTORS

Aerodyne Research, Inc.
ATTN: M. Camac

Aeronomy Corporation
ATTN: S. A. Bowhill

Aerospace Corporation
ATTN: V. Wall
ATTN: S. P. Bower
ATTN: D. C. Pecka
ATTN: R. D. Rawcliffe
ATTN: Julian Reinheimer
ATTN: M. Berg
ATTN: J. Woodford
ATTN: N. Cohen
ATTN: L. W. Aukerman
ATTN: Harris Mayer
ATTN: G. Millburn
ATTN: Thomas D. Taylor
ATTN: F. Keller
ATTN: George Paulikas
ATTN: T. Friedman
ATTN: J. Stevens
ATTN: V. Josephson
ATTN: J. Sorrels
ATTN: J. B. Blake

DEPARTMENT OF DEFENSE CONTRACTORS (Continued)

Analytical Systems Engineering Corp.
ATTN: J. A. Caruso

Battelle Memorial Institute
ATTN: Donald J. Hamman
ATTN: Radiation Eff. Info. Ctr.

The Boeing Company
ATTN: Glen Keister

The Trustees of Boston College
Chestnut Hill Campus
ATTN: R. Eather
ATTN: R. Hegblom
ATTN: R. L. Carovillao
ATTN: Lib. for Tech. Doc.
2 cy ATTN: Chairman Dept. of Chem.

Brown Engineering Company, Inc.
Cummings Research Park
ATTN: J. E. Cato
ATTN: J. Dobkins
ATTN: R. Deliberis
ATTN: Roland Patrick

University of California at Los Angeles
Office of Contract & Grant Admin.
ATTN: T. A. Farley, Space Sci. Ltr.

University of California at Riverside
ATTN: James N. Pitts, Jr.

University of California at San Diego
Marine Physical Lab. of the Scripps
Institute of Oceanography
ATTN: C. E. McIlwain, Physics Dept.
ATTN: S. C. Lin

University of California
Berkeley Campus, Room 318
ATTN: Kinsey A. Anderson

State of California
Air Resources Board
ATTN: Leo Zafonte

University of California
Space Sciences Laboratory
ATTN: Bodo Parady

Calspan Corporation
ATTN: Robert A. Fluegge
ATTN: W. Wurster
ATTN: M. G. Dunn
ATTN: Tech. Lib.
ATTN: C. E. Treanor

University of Colorado
Office of Contracts & Grants
ATTN: Jeffrey B. Pearce, LASP
ATTN: A. Phelps, JILA
ATTN: C. Lineberger, JILA
ATTN: Charles A. Barth, LASP

The Trustees of Columbia University
ATTN: Sec. Officer, W. M. Foley
ATTN: Richard N. Zare

DEPARTMENT OF DEFENSE CONTRACTORS (Continued)

Comsat Laboratories
ATTN: Doc. Con.

Computer Sciences Corp.
ATTN: C. Hulbert

Epsilon Laboratories, Inc.
ATTN: Henry Miranda
ATTN: Carl Accardo

ESL, Inc.
ATTN: James Marshall

General Dynamics Corporation
Inter-Division Research Laboratory
ATTN: Research Library

General Electric Company
Space Division
ATTN: F. Alyea
ATTN: Joseph C. Peden, VFSC, Rm. 4230M
ATTN: T. Bauer
ATTN: M. H. Bortner, Space Sci. Lab.
ATTN: P. Zavitsanos
ATTN: Tech. Info. Center

General Electric Company
TEMPO-Center for Advanced Studies
ATTN: B. Gambill
ATTN: Tim Stephens
ATTN: Don Chandler
ATTN: DASIAC
ATTN: Warren S. Knapp
5 cy ATTN: Mike Dudash

General Research Corporation
ATTN: John Ise, Jr.

General Research Corporation
ATTN: Thomas M. Zakrzewski

Geophysical Institute
University of Alaska
ATTN: J. S. Wagner, Physics Dept.
ATTN: R. Parthasarathy
ATTN: Tech. Lib.
ATTN: Neal Brown
ATTN: S. I. Akasofu
ATTN: T. N. Davis
ATTN: Henry Cole
ATTN: A. Belon

Grumman Aerospace Corporation
ATTN: Marton Rossi
ATTN: Michael D. Agostino

Harvard College Observatory
Smithsonian Astrophysical Observatory
Center for Astrophysics
ATTN: J. Patrick Henry

HRB-Singer, Inc.
ATTN: Tech. Info. Ctr., 650, F. J. McBride

HSS, Inc.
ATTN: M. P. Shuler
ATTN: Donald Hansen
ATTN: H. Stewart

DEPARTMENT OF DEFENSE CONTRACTORS (Continued)

IBM Corporation
ATTN: Tech. Rpts. Ctr. (912, A816)

IIT Research Institute
ATTN: Tech. Lib.

Institute for Defense Analyses
ATTN: Hans Wolfhard
ATTN: IDA Librarian, Ruth S. Smith
ATTN: Joel Bengston

Johns Hopkins University
Applied Physics Laboratory
ATTN: S. M. Krimigis
ATTN: Doc. Lib.
ATTN: Peter E. Partridge

Kaman Sciences Corporation
ATTN: Library
ATTN: Frank H. Shelton

Lockheed Missiles & Space Co., Inc.
ATTN: S. I. Weiss, D/68-01
ATTN: Edwin A. Smith, Dept. 85-85
ATTN: E. E. Crowther, D/60-01
ATTN: D. L. Crowther, D/62-25
ATTN: J. T. Hart, Jr., D/61-03
ATTN: J. H. Hockenberry, D/60-01
ATTN: Q. A. Riepe, D/60-80
ATTN: D. R. Churchill
ATTN: D. F. McClinton
ATTN: J. Cretcher

Lockheed Missiles & Space Co., Inc.
ATTN: W. L. Imhof, D/52-12
ATTN: T. D. Dassell
ATTN: G. H. Nakano
ATTN: W. D. Frye, D/52-21
ATTN: R. A. Breuch, D/52-21
ATTN: James W. Schallau
ATTN: J. B. Reagan, D/52-12
ATTN: R. K. Landshoff
ATTN: Tech. Info. Ctr., D/Coll.
ATTN: Richard G. Johnson, Dept. 52-12
ATTN: R. P. Caren, D/52-20
ATTN: R. D. Sharp, D/52-12
ATTN: A. D. Anderson, D/52-12
ATTN: John E. Evans, Dept. 52-14
ATTN: D. C. Fisher, D/52-14
ATTN: Billy M. McCormac, Dept. 52-54
ATTN: Martin Walt, Dept. 52-10
ATTN: L. L. Newkirk, D/52-21
ATTN: John B. Cladis, Dept. 52-12
ATTN: W. E. Francis, D/52-12
ATTN: G. T. Davidson, D/52-12

Maxwell Laboratories, Inc.
ATTN: Victor Fargo

McDonnell Douglas Corporation
ATTN: William Olson
ATTN: A. D. Goedeke

University of Minnesota
ATTN: J. R. Winkler

DEPARTMENT OF DEFENSE CONTRACTORS (Continued)

Mission Research Corporation
ATTN: Dave Sowle
ATTN: M. Scheibe
ATTN: D. Sappenfield
ATTN: D. Archer
ATTN: Conrad L. Longmire
ATTN: R. Hendrick

The Mitre Corporation
ATTN: Tech. Lib. for B. Troutman
ATTN: P. Grant
ATTN: Tech. Lib. for R. Greeley

National Academy of Sciences
3 cy ATTN: National Materials Advisory Board
for William C. Bartley/Edward R. Dyer/
J. R. Sievers

Pennsylvania State University
Industrial Security Office
ATTN: L. Hale
ATTN: J. S. Nisbet

Photometrics, Inc.
ATTN: Irving L. Kofsky

Physical Dynamics, Inc.
ATTN: A. Thompson
ATTN: Joseph B. Workman

Physical Sciences, Inc.
ATTN: Kurt Wray
ATTN: R. L. Taylor

University of Pittsburgh of the
Comwlth. Sys. of Higher Educ.
Cathedral of Learning
ATTN: Manfred A. Biondi
ATTN: Frederick Kaufman

R&D Associates
ATTN: Robert E. Lelevier
ATTN: William J. Karzas
ATTN: R. P. Turco
ATTN: William R. Graham, Jr.
ATTN: R. G. Lindgren
ATTN: Forrest Gilmore
ATTN: Albert L. Latter
ATTN: H. A. Dry

R&D Associates
ATTN: Herbert J. Mitchell

The Rand Corporation
ATTN: Cullen Crain
ATTN: Technical Library
ATTN: Paul Tamarkin

Rice University
Department of Space Science
ATTN: Ronald F. Stebbings
ATTN: Joseph Chamberlain

Rockwell International Corporation
ATTN: William Atwell

Sanders Associates, Inc.
ATTN: Jack Schwartz

DEPARTMENT OF DEFENSE CONTRACTORS (Continued)

Science Applications, Inc.

ATTN: D. Sachs
ATTN: Daniel A. Hamlin

Professor Chalmers F. Sechrist

ATTN: C. Sechrist

Smithsonian Astrophysical Observatory

ATTN: A. Dalgarno

University of Southern California

ATTN: S. W. Benson

Space Data Corporation

ATTN: Edward F. Allen

SRI International

ATTN: G. Black
ATTN: James R. Peterson
ATTN: L. L. Cobb
ATTN: M. Baron
ATTN: R. D. Hake, Jr.
ATTN: Ray L. Leadabrand
ATTN: Ronald White
ATTN: Walter G. Chesnut
ATTN: Felix T. Smith
ATTN: Allen M. Peterson
ATTN: E. Kindermann
ATTN: J. Lomax
ATTN: Arthur Lee Whitson
ATTN: Burt R. Gasten

SRI International

ATTN: Warren W. Berning

Stanford University

Radio Science Laboratory
ATTN: R. A. Helliwell
ATTN: D. L. Carpenter

DEPARTMENT OF DEFENSE CONTRACTORS (Continued)

Technology International Corporation

ATTN: W. P. Boquist

TRW Defense & Space Sys. Group

ATTN: F. Scarf, R5-1280
ATTN: J. F. Friichtenicht, RI-1196
ATTN: H. H. Holloway, RI-2036
ATTN: O. F. Adams, RI-1144
ATTN: Tech. Info. Center/S-1930
ATTN: R. K. Plebuch, RI-2078
ATTN: R. Watson, RI/1096

United Technologies Corporation

ATTN: Robert H. Bullis
ATTN: H. Michels

Utah State University

ATTN: C. Wyatt
ATTN: Doran Baker
ATTN: Kay Baker
ATTN: D. Burt

Visidyne, Inc.

ATTN: J. W. Carpenter

Wayne State University

ATTN: Pieter K. Rol, Chem. Engrg. & Mat. Sci.
ATTN: R. H. Kummller

Wayne State University

Department of Physics
ATTN: Walter E. Kauppila